Title

Minimizing L 1 over L 2 norms on the gradient

Journal

Inverse Problems, 38(6)

ISSN

0266-5611

Authors

Wang, Chao
Tao, Min
Chuah, Chen-Nee
et al.

Publication Date

2022-06-01

DOI

10.1088/1361-6420/ac64fb

Peer reviewed

HHS Public Access
Author manuscript
Inverse Probl. Author manuscript; available in PMC 2023 June 01.

Published in final edited form as:
Inverse Probl. 2022 June ; 38(6): .

Minimizing L_1 over L_2 norms on the gradient

Chao Wang[1,2], **Min Tao**[3], **Chen-Nee Chuah**[2], **James Nagy**[4], **Yifei Lou**[5]

[1]Department of Statistic and Data Science, Southern University of Science and Technology, Shenzhen 518055, China

[2]Department of Electrical and Computer Engineering, University of California Davis, Davis, CA 95616, USA

[3]Department of Mathematics, National Key Laboratory for Novel Software Technology, Nanjing University, Nanjing 210093, China

[4]Department of Mathematics, Emory University, Atlanta, GA 30322, USA

[5]Department of Mathematical Sciences, University of Texas at Dallas, Richardson, TX 75080, USA

Abstract

In this paper, we study the L_1/L_2 minimization on the gradient for imaging applications. Several recent works have demonstrated that L_1/L_2 is better than the L_1 norm when approximating the L_0 norm to promote sparsity. Consequently, we postulate that applying L_1/L_2 on the gradient is better than the classic total variation (the L_1 norm on the gradient) to enforce the sparsity of the image gradient. Numerically, we design a specific splitting scheme, under which we can prove subsequential and global convergence for the alternating direction method of multipliers (ADMM) under certain conditions. Experimentally, we demonstrate visible improvements of L_1/L_2 over L_1 and other nonconvex regularizations for image recovery from low-frequency measurements and two medical applications of MRI and CT reconstruction. Finally, we reveal some empirical evidence on the superiority of L_1/L_2 over L_1 when recovering piecewise constant signals from low-frequency measurements to shed light on future works.

Keywords

L_1/L_2 minimization; piecewise constant images; alternating direction method of multipliers; global convergence

1. Introduction

Regularization methods play an important role in inverse problems to refine the solution space by prior knowledge and/or special structures. For example, the celebrated total variation (TV) [1] prefers piecewise constant images, while total generalized variation (TGV) [2] and fractional-order TV [3, 4] tend to preserve piecewise smoothness of an

chaowang.hk@gmail.com .

image. TV can be defined either isotropically or anisotropically. The anisotropic TV [5] in the discrete setting is equivalent to applying the L_1 norm on the image gradient. As the L_1 norm is often used to enforce a signal being *sparse,* one can interpret the TV regularization as to promote the sparsity of gradient vectors.

To find the sparsest signal, it is straightforward to minimize the L_0 norm (counting the number of nonzero elements), which is unfortunately NP-hard [6]. A popular approach involves the convex relaxation of using the L_1 norm to replace the ill-posed L_0 norm, with the equivalence between L_1 and L_0 for sparse signal recovery given in terms of restricted isometry property (RIP) [7]. However, Fan and Li [8] pointed out that the L_1 approach is biased towards large coefficients, and proposed to minimize a nonconvex regularization, called smoothly clipped absolute deviation (SCAD). Subsequently, various nonconvex functionals emerged such as minimax concave penalty (MCP) [9], capped L_1 [10, 11, 12], and transformed L_1 [13, 14, 15]. Following the literature on sparse signal recovery, there is a trend to apply a nonconvex regularization on the gradient to deal with images. For instance, Chartrand [16] discussed both the L_p norm with $0 < p < 1$ for sparse signals and L_p on the gradient for magnetic resonance imaging (MRI), while MCP on the gradient was proposed in [17].

Recently, a scale-invariant functional L_1/L_2 was examined, which gives promising results in recovering sparse signals [18, 19, 20] and sparse gradients [21]. In this paper, we rely on a constrained formulation to characterize some scenarios, under which the quotient of the L_1 and L_2 norms on the gradient performs well. Numerically, we consider the same splitting scheme used in an unconstrained formulation [21] to minimize the L_1/L_2 on the gradient, followed by the alternating direction method of multipliers (ADMM) [22]. We formulate the linear constraint using an indicator function and utilize the optimality conditions for constrained optimization problems to prove that the sequence generated by the proposed algorithm converges to a stationary point, referred to as *global convergence*.

We present some algorithmic insights on computational efficiency of our proposed algorithm for nonconvex optimization. Specifically, we discuss algorithmic behaviors on two types of applications: MRI and computed tomography (CT). For the MRI reconstruction, a subproblem in ADMM has a closed-form solution, while an iterative solver is required for CT. As the accuracy of the subproblem varies between MRI and CT, we shall alter internal settings of our algorithm accordingly. In summary, this paper relies on a constrained formulation to discuss theoretical and computational aspects of a nonconvex regularization for imaging problems. The major contributions are two-fold: (i) We establish the global convergence of the proposed algorithm under the certain assumptions. (ii) We conduct extensive experiments to characterize computational efficiency of our algorithm and discuss how internal settings can be customized to cater to specific imaging applications, such as MRI and limited-angle CT reconstruction. Numerical results highlight the superior performance of our approach over other gradient-based regularizations.

The rest of the paper is organized as follows. Section 2 defines the notations that will be used through the paper, and gives a brief review on the related works. The numerical scheme is detailed in Section 3, followed by convergence analysis in Section 4. Section 5 presents three types of imaging applications: super-resolution, MRI and CT reconstruction problems. Section 6 discusses some empirical evidences for TV's exact recovery and advantages of the proposed model. Finally, conclusions and future works are given in Section 7.

2. Preliminaries

We use a bold letter to denote a vector, a capital letter to denote a matrix or linear operator, and a calligraphic letter for a vector space. We use ⊙ to denote the component-wise multiplication of two vectors. When a function (e.g., sign, max, min) applies to a vector, it returns a vector with corresponding component-wise operation.

We adopt a discrete setting to describe the related models. Suppose a two-dimensional (2D) image is defined on an $m \times n$ Cartesian grid. By using a standard linear index, we can represent a 2D image as a vector, i.e., the $((i-1)m + j)$-th component denotes the intensity value at pixel (i, j). We define a discrete gradient operator,

$$D\mathbf{u} := \begin{bmatrix} D_x \\ D_y \end{bmatrix} \mathbf{u}, \tag{1}$$

where D_x, D_y are the finite forward difference operator with periodic boundary condition in the horizontal and vertical directions, respectively. We denote $N := mn$ and the Euclidean spaces by $\mathcal{X} := \mathbb{R}^N$, $\mathcal{Y} := \mathbb{R}^{2N}$, then $\mathbf{u} \in \mathcal{X}$ and $D\mathbf{u} \in \mathcal{Y}$. We can apply the standard norms, e.g., L_1, L_2, on vectors $\mathbf{u}$ and $D\mathbf{u}$. For example, the L_1 norm on the gradient, i.e., $\|D\mathbf{u}\|_1$, is the anisotropic TV regularization functional [5]. Throughout the paper, we use TV and "L_1 on the gradient" interchangeably.

We examine the L_1/L_2 penalty on the gradient in a constrained formulation,

$$\min_{\mathbf{u}} \frac{\|D\mathbf{u}\|_1}{\|D\mathbf{u}\|_2} \quad \text{s.t.} \quad A\mathbf{u} = \mathbf{b}. \tag{2}$$

One way to solve for (2) involves the following equivalent form

$$\min_{\mathbf{u}, \mathbf{d}, \mathbf{h}} \frac{\|\mathbf{d}\|_1}{\|\mathbf{h}\|_2} \quad \text{s.t.} \quad A\mathbf{u} = \mathbf{b}, \ \mathbf{d} = D\mathbf{u}, \quad \mathbf{h} = D\mathbf{u}, \tag{3}$$

with two auxiliary variables $\mathbf{d}$ and $\mathbf{h}$. For more details, please refer to [18] that presented a proof-of-concept example for MRI reconstruction. An alternative approach was discussed in our preliminary work [21] for an unconstrained minimization problem,

$$\min_{\mathbf{u}, \mathbf{h}} \frac{\|D\mathbf{u}\|_1}{\|\mathbf{h}\|_2} + \frac{\lambda}{2}\|A\mathbf{u} - \mathbf{b}\|_2^2 \quad \text{s.t.} \quad \mathbf{h} = D\mathbf{u}, \tag{4}$$

where $\lambda > 0$ is a weighting parameter. By only introducing one variable $\mathbf{h}$, the new splitting scheme (4) can guarantee subsequential/global convergence of the ADMM framework under certain conditions.

In this paper, we utilize the splitting scheme (4) to solve the constrained problem (2), which is crucial to reveal theoretical properties of the gradient-based regularizations for image reconstruction, as elaborated in Section 6. It is true that the constrained formulation limits our experimental design in a noise-free fashion, but it helps us to draw conclusions solely on the model, ruling out any influence from other nuisances such as noises and tuning parameters. Our model (2) is parameter-free, while there is a parameter λ in the unconstrained problem (4).

3. The proposed approach

Starting from (2), we incorporate an additional box constraint in the model, i.e.,

$$\min_{\mathbf{u}} \frac{\| D\mathbf{u}\|_1}{\| D\mathbf{u}\|_2} \quad \text{s.t.} \quad A\mathbf{u} = \mathbf{b}, \quad \mathbf{u} \in [p, q]^N. \tag{5}$$

The notation $\mathbf{u} \in [p, q]^N$ means that every element of $\mathbf{u}$ is bounded by $[p, q]$. The box constraint is reasonable for image processing applications [23, 24], since pixel values are usually bounded by [0, 1] or [0, 255]. On the other hand, the box constraint is particularly helpful for the L_1/L_2 model to prevent its divergence [19].

We use the indicator function to rewrite (5) into the following equivalent form

$$\min_{\mathbf{u},\mathbf{h}} \frac{\| D\mathbf{u}\|_1}{\| \mathbf{h}\|_2} + \prod\nolimits_{A\mathbf{u}=\mathbf{b}}(\mathbf{u}) + \prod\nolimits_{[p,q]^N}(\mathbf{u}) \quad \text{s.t.} \quad D\mathbf{u} = \mathbf{h}, \tag{6}$$

where $\prod_S(\mathrm{t})$ denotes the indicator function that forces $\mathbf{t}$ to belong to a feasible set S, i.e.,

$$\prod\nolimits_S(\mathbf{t}) = \begin{cases} 0 & \text{if } \mathbf{t} \in S \\ +\infty & \text{otherwise.} \end{cases} \tag{7}$$

The augmented Lagrangian function corresponding to (6) can be expressed as,

$$\mathscr{L}(\mathbf{u}, \mathbf{h}; \mathbf{g}) = \frac{\| D\mathbf{u}\|_1}{\| \mathbf{h}\|_2} + \prod\nolimits_{A\mathbf{u}=\mathbf{b}}(\mathbf{u}) + \prod\nolimits_{[p,q]^N}(\mathbf{u}) + \langle \rho \mathbf{g}, D\mathbf{u} - \mathbf{h}\rangle + \frac{\rho}{2}\| D\mathbf{u} - \mathbf{h}\|_2^2, \tag{8}$$

where $\mathbf{g}$ is a dual variable and ρ is a positive parameter. Then ADMM iterates as follows,

$$\begin{cases} \mathbf{u}^{(k+1)} = \text{argmin}_{\mathbf{u}} \mathscr{L}\left(\mathbf{u}, \mathbf{h}^{(k)}; \mathbf{g}^{(k)}\right) \\ \mathbf{h}^{(k+1)} = \text{argmin}_{\mathbf{h}} \mathscr{L}\left(\mathbf{u}^{(k+1)}, \mathbf{h}; \mathbf{g}^{(k)}\right) \\ \mathbf{g}^{(k+1)} = \mathbf{g}^{(k)} + D\mathbf{u}^{(k+1)} - \mathbf{h}^{(k+1)}. \end{cases} \tag{9}$$

The update for **h** is the same as in [18], which has a closed-form solution of

$$\mathbf{h}^{(k+1)} = \begin{cases} \tau^{(k)}\left(D\mathbf{u}^{(k+1)} + \mathbf{g}^{(k)}\right) & \text{if } D\mathbf{u}^{(k+1)} + \mathbf{g}^{(k)} \neq \mathbf{0} \\ \mathbf{r}^{(k)} & \text{otherwise,} \end{cases} \tag{10}$$

where $\mathbf{r}^{(k)}$ is a random vector with the L_2 norm being $\sqrt[3]{\frac{\|D\mathbf{u}^{(k+1)}\|_1}{\rho}}$ and $\tau^{(k)} = \frac{1}{3} + \frac{1}{3}\left(\xi^{(k)} + \frac{1}{\xi^{(k)}}\right)$ for

$$\xi^{(k)} = \sqrt[3]{\frac{27\eta^{(k)} + 2 + \sqrt{\left(27\eta^{(k)} + 2\right)^2 - 4}}{2}} \quad \text{and} \quad \eta^{(k)} = \frac{\|D\mathbf{u}^{(k+1)}\|_1}{\rho\|D\mathbf{u}^{(k+1)} + \mathbf{g}^{(k)}\|_2^3}.$$

We elaborate on the **u**-subproblem in (9), which can be expressed by the box constraint, i.e.,

$$\mathbf{u}^{(k+1)} = \underset{\mathbf{u}}{\text{argmin}} \frac{\|D\mathbf{u}\|_1}{\|\mathbf{h}^{(k)}\|_2} + \frac{\rho}{2}\|D\mathbf{u} - \mathbf{h}^{(k)} + \mathbf{g}^{(k)}\|_2^2 \quad \text{s.t.} \quad A\mathbf{u} = \mathbf{b}, \ \ \mathbf{u} \in [p, q]^N. \tag{11}$$

To solve for (11), we introduce two variables, **v** for the box constraint and **d** for the gradient, thus getting

$$\min_{\mathbf{u}, \mathbf{d}, \mathbf{v}} \frac{\|\mathbf{d}\|_1}{\|\mathbf{h}^{(k)}\|_2} + \frac{\rho}{2}\|D\mathbf{u} - \mathbf{h}^{(k)} + \mathbf{g}^{(k)}\|_2^2 + \prod_{[p,q]^N}(\mathbf{v}) \quad \text{s.t.} \quad \mathbf{u} = \mathbf{v}, \ \ D\mathbf{u} = \mathbf{d}, \ \ A\mathbf{u} = \mathbf{b}. \tag{12}$$

The augmented Lagrangian function corresponding to (12) becomes

$$\begin{aligned} \mathscr{L}^{(k)}(\mathbf{u}, \mathbf{d}, \mathbf{v}; \mathbf{w}, \mathbf{y}, \mathbf{z}) = & \frac{\|\mathbf{d}\|_1}{\|\mathbf{h}^{(k)}\|_2} + \frac{\rho}{2}\|D\mathbf{u} - \mathbf{h}^{(k)} + \mathbf{g}^{(k)}\|_2^2 + \prod_{[p,q]^N}(\mathbf{v}) \\ & + \langle \beta\mathbf{w}, \mathbf{u} - \mathbf{v}\rangle + \frac{\beta}{2}\|\mathbf{u} - \mathbf{v}\|_2^2 \\ & + \langle \gamma\mathbf{y}, D\mathbf{u} - \mathbf{d}\rangle + \frac{\gamma}{2}\|D\mathbf{u} - \mathbf{d}\|_2^2 \\ & + \langle \lambda\mathbf{z}, A\mathbf{u} - \mathbf{b}\rangle + \frac{\lambda}{2}\|A\mathbf{u} - \mathbf{b}\|_2^2, \end{aligned} \tag{13}$$

where $\mathbf{w}$, $\mathbf{y}$, $\mathbf{z}$ are dual variables and β, γ, λ are positive parameters. Here we have k in the superscript of $\mathscr{L}$ to indicate that it is the Lagrangian for the $\mathbf{u}$-subproblem in (9) at the kth iteration. The ADMM framework to minimize (12) leads to

$$\begin{cases} \mathbf{u}_{j+1} = \operatorname{argmin}_{\mathbf{u}} \mathscr{L}^{(k)}(\mathbf{u}, \mathbf{d}_j, \mathbf{v}_j; \mathbf{w}_j, \mathbf{y}_j, \mathbf{z}_j) \\ \mathbf{d}_{j+1} = \operatorname{argmin}_{\mathbf{d}} \mathscr{L}^{(k)}(\mathbf{u}_{j+1}, \mathbf{d}, \mathbf{v}_j; \mathbf{w}_j, \mathbf{y}_j, \mathbf{z}_j) \\ \mathbf{v}_{j+1} = \operatorname{argmin}_{\mathbf{v}} \mathscr{L}^{(k)}(\mathbf{u}_{j+1}, \mathbf{d}_{j+1}, \mathbf{v}; \mathbf{w}_j, \mathbf{y}_j, \mathbf{z}_j) \\ \mathbf{w}_{j+1} = \mathbf{w}_j + \mathbf{u}_{j+1} - \mathbf{v}_{j+1} \\ \mathbf{y}_{j+1} = \mathbf{y}_j + D\mathbf{u}_{j+1} - \mathbf{d}_{j+1} \\ \mathbf{z}_{j+1} = \mathbf{z}_j + A\mathbf{u}_{j+1} - \mathbf{b}, \end{cases} \tag{14}$$

where the subscript j represents the inner loop index, as opposed to the superscript k for outer iterations in (9). By taking derivative of $\mathscr{L}^{(k)}$ with respect to $\mathbf{u}$, we obtain a closed-form solution,

$$\begin{aligned} \mathbf{u}_{j+1} = & \left(\lambda A^T A + (\rho + \gamma) D^T D + \beta I\right)^{-1} \Big(\lambda A^T (\mathbf{b} - \mathbf{z}_j) \\ & + \gamma D^T (\mathbf{d}_j - \mathbf{y}_j) + \rho D^T \left(\mathbf{h}^{(k)} - \mathbf{g}^{(k)}\right) + \beta (\mathbf{v}_j - \mathbf{w}_j)\Big), \end{aligned} \tag{15}$$

Algorithm 1 The L_1/L_2 minimization on the gradient

Input: a linear operator A, observed data $\mathbf{b}$, and a bound $[p, q]$ for the original image
Parameters: $\rho, \lambda, \gamma, \beta$, kMax, jMax, and $\epsilon \in \mathbb{R}$
Initialize: $\mathbf{h}$, $\mathbf{d}$, $\mathbf{g}$, $\mathbf{v}, \mathbf{w}$, $\mathbf{y}$, $\mathbf{z} = \mathbf{0}$, and $k, j = 0$
while $k <$ kMax or $\|\mathbf{u}^{(k)} - \mathbf{u}^{(k-1)}\|_2 / \|\mathbf{u}^{(k)}\|_2 > \epsilon$ **do**
  while $j <$ jMax or $\|\mathbf{u}_j - \mathbf{u}_{j-1}\|_2 / \|\mathbf{u}_j\|_2 > \epsilon$ **do**
    $\mathbf{u}_{j+1} = \left(\lambda A^T A + (\rho + \gamma) D^T D + \beta I\right)^{-1} \Big(\lambda A^T (\mathbf{b} - \mathbf{z}_j) + \gamma D^T (\mathbf{d}_j - \mathbf{y}_j) + \rho D^T \left(\mathbf{h}^{(k)} - \mathbf{g}^{(k)}\right) + \beta (\mathbf{v}_j - \mathbf{w}_j)\Big)$
    $\mathbf{d}_{j+1} = \mathbf{shrink}\left(D\mathbf{u}_{j+1} + \mathbf{y}_j, \frac{1}{\gamma \|\mathbf{h}^{(k)}\|_2}\right)$
    $\mathbf{v}_{j+1} = \min\{\max\{\mathbf{u}_{j+1} + \mathbf{w}_j, p\}, q\}$
    $\mathbf{w}_{j+1} = \mathbf{w}_j + \mathbf{u}_{j+1} - \mathbf{v}_{j+1}$
    $\mathbf{y}_{j+1} = \mathbf{y}_j + D\mathbf{u}_{j+1} - \mathbf{d}_{j+1}$
    $\mathbf{z}_{j+1} = \mathbf{z}_j + A\mathbf{u}_{j+1} - \mathbf{b}$
    Assign j by $j + 1$
  end while
  Set $\mathbf{u}^{(k+1)}$ as $\mathbf{u}_j$
  Update $\mathbf{h}^{(k+1)}$ by (10)
  $\mathbf{g}^{(k+1)} = \mathbf{g}^{(k)} + D\mathbf{u}^{(k+1)} - \mathbf{h}^{(k+1)}$
  Assign k and j by $k + 1$ and 0, respectively
end while
return $\mathbf{u}^* = \mathbf{u}^{(k)}$

where I stands for the identity matrix. When the matrix A involves frequency measurements, e.g., in super-resolution and MRI reconstruction, the update in (15) can be implemented efficiently by the fast Fourier transform (FFT) for the periodic boundary condition when defining the derivative operator D in (1). For a general system matrix A, we adopt the conjugate gradient descent [25] to solve for (15).

The **d**-subproblem in (14) also has a closed-form solution, i.e.,

$$\mathbf{d}_{j+1} = \mathbf{shrink}\left(D\mathbf{u}_{j+1} + \mathbf{y}_j, \frac{1}{\gamma\|\mathbf{h}^{(k)}\|_2}\right), \tag{16}$$

where $\mathbf{shrink}(\mathbf{x}, \mu) = \text{sign}(\mathbf{x}) \odot \max\{|\mathbf{x}| - \mu, 0\}$ is called *soft shrinkage* and $\odot$ denotes element-wise multiplication. We update **v** by a projection onto the $[p, q]$-box constraint, which is given by

$$\mathbf{v}_{j+1} = \min\{\max\{\mathbf{u}_{j+1} + \mathbf{w}_j, p\}, q\}.$$

In summary, we present an ADMM-based algorithm to minimize the L_1/L_2 on the gradient subject to a linear system with the box constraint in Algorithm 1.

4. Convergence analysis

We intend to establish the convergence of Algorithm 1 with the box constraint, which is extensively tested in the experiments. Since our ADMM framework (9) share the same structure with the unconstrained formulation (4), we adapt some analysis in [21] to prove the subsequential convergence for the proposed model (5). For example, we make Assumption 1, which is the same as in [21].

Assumption 1. $\mathcal{N}(D) \cap \mathcal{N}(A) = \{\mathbf{0}\}$, *where* $\mathcal{N}$ *denotes the null space and* D *is defined in* (1). *In addition, the norm of* $\{\mathbf{h}^{(k)}\}$ *generated by* (9) *has a lower bound, i.e., there exists a positive constant* ϵ *such that* $\|\mathbf{h}^{(k)}\|_2 \geq \epsilon, \ \forall k$.

Remark 1. *We have* $\|\mathbf{h}\|_2 > 0$ *in the* L_1/L_2 *model as the denominator shall not be zero. It is true that* $\|\mathbf{h}\|_2 > 0$ *does not imply a uniform lower bound of* ϵ *such that* $\|\mathbf{h}\|_2 > \epsilon$ *in Assumption 1. Here we can redefine the divergence of an algorithm by including the case of* $\|\mathbf{h}^{(k)}\|_2 < \epsilon$, *which can be checked numerically with a pre-set value of* ϵ.

To avoid redundancies as in [21], we focus on different strategies in proving convergence for the constrained problem, such as optimality conditions and subgradient of the indicator function. In particular, we consider the following modified augmented Lagrangian by incorporating the lower bound of $\|\mathbf{h}\|_2$, i.e.,

$$\begin{aligned}\mathcal{L}_\epsilon(\mathbf{u},\mathbf{h};\mathbf{g}) = \frac{\|D\mathbf{u}\|_1}{\|\mathbf{h}\|_2} + \prod\nolimits_{A\mathbf{u}=\mathbf{b}}(\mathbf{u}) + \prod\nolimits_{[p,q]^N}(\mathbf{u}) + \prod\nolimits_{\|\mathbf{h}\|_2 \geq \epsilon/2}(\mathbf{h}) \\ + \langle \rho\mathbf{g}, D\mathbf{u} - \mathbf{h}\rangle + \frac{\rho}{2}\|D\mathbf{u} - \mathbf{h}\|_2^2.\end{aligned} \tag{17}$$

Under Assumption 1 (specifically $\|\mathbf{h}\|_2 \geq \epsilon$), we have $\mathscr{L}_\epsilon = \mathscr{L}$. We further show that $\mathscr{L}_\epsilon$ has the Kurdyka-Łojasiewicz (KL) property [26], and hence the global convergence of ADMM can be established.

Lemma 1. *(sufficient descent) Under Assumption 1 and a sufficiently large ρ, the sequence* $\{\mathbf{u}^{(k)}, \mathbf{h}^{(k)}, \mathbf{g}^{(k)}\}$ *generated by* (9) *satisfies*

$$\mathscr{L}\left(\mathbf{u}^{(k+1)}, \mathbf{h}^{(k+1)}; \mathbf{g}^{(k+1)}\right) \leq \mathscr{L}\left(\mathbf{u}^{(k)}, \mathbf{h}^{(k)}; \mathbf{g}^{(k)}\right) - c_1\|\mathbf{u}^{(k+1)} - \mathbf{u}^{(k)}\|_2^2 - c_2\|\mathbf{h}^{(k+1)} - \mathbf{h}^{(k)}\|_2^2, \tag{18}$$

where c_1 and c_2 are two positive constants.

Proof. Denote σ as the smallest eigenvalue of the matrix $A^TA + D^TD$. We show σ is strictly positive. If $\sigma = 0$, there exists a nonzero vector $\mathbf{x}$ such that $\mathbf{x}^T(A^TA + D^TD)\mathbf{x} = 0$. It is straightforward that $\mathbf{x}^TA^TA\mathbf{x} \geq 0$ and $\mathbf{x}^TD^TD\mathbf{x} \geq 0$, so one shall have $\mathbf{x}^TA^TA\mathbf{x} = 0$ and $\mathbf{x}^TD^TD\mathbf{x} = 0$, which contradicts $\mathscr{N}(D) \cap \mathscr{N}(A) = \{\mathbf{0}\}$ in Assumption 1. Therefore, there exists a positive $\sigma > 0$ such that

$$\mathbf{v}^T\left(A^TA + D^TD\right)\mathbf{v} \geq \sigma\|\mathbf{v}\|_2^2, \quad \forall \mathbf{v}.$$

By letting $\mathbf{v} = \mathbf{u}^{(k+1)} - \mathbf{u}^{(k)}$ and using $A\mathbf{u}^{(k+1)} = A\mathbf{u}^{(k)} = \mathbf{b}$, we have

$$\left\|D\left(\mathbf{u}^{(k+1)} - \mathbf{u}^{(k)}\right)\right\|_2^2 \geq \sigma\|\mathbf{u}^{(k+1)} - \mathbf{u}^{(k)}\|_2^2. \tag{19}$$

We express the $\mathbf{u}$-subproblem in (9) equivalently as

$$\begin{aligned} \mathbf{u}^{(k+1)} = \operatorname*{argmin}_{\mathbf{u}} & \frac{\|D\mathbf{u}\|_1}{\|\mathbf{h}^{(k)}\|_2} + \frac{\rho}{2}\|D\mathbf{u} - \mathbf{h}^{(k)} + \mathbf{g}^{(k)}\|_2^2 \\ \text{s.t.} \quad & A\mathbf{u} = \mathbf{b}, \; p - \mathbf{u} \leq \mathbf{0}, \text{ and } \mathbf{u} - q \leq \mathbf{0}. \end{aligned} \tag{20}$$

The optimality conditions state that $A\mathbf{u}^{(k+1)} = \mathbf{b}$ and there exist three sets of vectors $\mathbf{w}_i$ (i = 1, 2, 3) and $\mathbf{p}^{(k+1)} \in \partial\|D\mathbf{u}^{(k+1)}\|_1$ such that

$$\mathbf{0} = \frac{\mathbf{p}^{(k+1)}}{\|\mathbf{h}^{(k)}\|_2} + \rho D^T\left(D\mathbf{u}^{(k+1)} - \mathbf{h}^{(k)} + \mathbf{g}^{(k)}\right) + A^T\mathbf{w}_1 - \mathbf{w}_2 + \mathbf{w}_3. \tag{21}$$

By the complementary slackness, we have $\mathbf{w}_2, \mathbf{w}_3 \geq \mathbf{0}$ and

$$\left(p - \mathbf{u}^{(k+1)}\right) \odot \mathbf{w}_2 = \left(\mathbf{u}^{(k+1)} - q\right) \odot \mathbf{w}_3 = \mathbf{0}, \tag{22}$$

which implies that

$$\left\langle \mathbf{w}_2, \mathbf{u}^{(k+1)} - \mathbf{u}^{(k)} \right\rangle = \left\langle \mathbf{w}_2, \mathbf{u}^{(k+1)} - p + p - \mathbf{u}^{(k)} \right\rangle = \left\langle \mathbf{w}_2, p - \mathbf{u}^{(k)} \right\rangle \leq 0.$$

Similarly, we have $\langle \mathbf{w}_2, \mathbf{u}^{(k+1)} - \mathbf{u}^{(k)} \rangle \geq 0$ for $\mathbf{w}_3$. Using the subgradient definition, $A\mathbf{u}^{(k+1)} = A\mathbf{u}^{(k)} = \mathbf{b}$, and (19)–(22), we obtain that

$$
\begin{aligned}
&\mathscr{L}\left(\mathbf{u}^{(k+1)}, \mathbf{h}^{(k)}; \mathbf{g}^{(k)}\right) - \mathscr{L}\left(\mathbf{u}^{(k)}, \mathbf{h}^{(k)}; \mathbf{g}^{(k)}\right) \\
&\leq \left\langle \frac{\mathbf{p}^{(k+1)}}{\|\mathbf{h}^{(k)}\|_2}, \mathbf{u}^{(k+1)} - \mathbf{u}^{(k)} \right\rangle + \frac{\rho}{2}\|D\mathbf{u}^{(k+1)} - \mathbf{f}^{(k)}\|_2^2 - \frac{\rho}{2}\|D\mathbf{u}^{(k)} - \mathbf{f}^{(k)}\|_2^2 \\
&= -\left\langle \mathbf{w}_1, A\mathbf{u}^{(k+1)} - A\mathbf{u}^{(k)} \right\rangle + \left\langle \mathbf{w}_2, \mathbf{u}^{(k+1)} - \mathbf{u}^{(k)} \right\rangle - \left\langle \mathbf{w}_3, \mathbf{u}^{(k+1)} - \mathbf{u}^{(k)} \right\rangle \\
&\quad -\rho\left\langle D\mathbf{u}^{(k+1)} - \mathbf{f}^{(k)}, D\mathbf{u}^{(k+1)} - D\mathbf{u}^{(k)} \right\rangle + \frac{\rho}{2}\|D\mathbf{u}^{(k+1)} - \mathbf{f}^{(k)}\|_2^2 - \frac{\rho}{2}\|D\mathbf{u}^{(k)} - \mathbf{f}^{(k)}\|_2^2 \\
&\leq -\frac{\rho}{2}\|D\mathbf{u}^{(k+1)} - D\mathbf{u}^{(k)}\|_2^2 \leq -\frac{\sigma\rho}{2}\|\mathbf{u}^{(k+1)} - \mathbf{u}^{(k)}\|_2^2,
\end{aligned}
$$

where $\mathbf{f}^{(k)} = \mathbf{h}^{(k)} - \mathbf{g}^{(k)}$. The bounds of $\mathscr{L}\left(\mathbf{u}^{(k+1)}, \mathbf{h}^{(k+1)}; \mathbf{g}^{(k)}\right) - \mathscr{L}\left(\mathbf{u}^{(k+1)}, \mathbf{h}^{(k)}; \mathbf{g}^{(k)}\right)$ and $\mathscr{L}\left(\mathbf{u}^{(k+1)}, \mathbf{h}^{(k+1)}; \mathbf{g}^{(k+1)}\right) - \mathscr{L}\left(\mathbf{u}^{(k+1)}, \mathbf{h}^{(k+1)}; \mathbf{g}^{(k)}\right)$ exactly follow [21, Lemma 4.3] for the unconstrained formulation, and hence we omit the rest of the proof. ☐

Remark 2. *Lemma 1 requires ρ to be sufficiently large so that two parameters c_1 and c_2 are positive. Following the proof of* [21, *Lemma 4.3], c_1 and c_2 can be explicitly expressed as*

$$c_1 = \frac{\sigma\rho}{2} - \frac{16N}{\rho\epsilon^4} \quad \textit{and} \quad c_2 = \frac{\rho\epsilon^3 - 6M}{2\epsilon^3} - \frac{16M^2}{\rho\epsilon^6}, \tag{23}$$

where $M = \sup_k \|D\mathbf{u}^{(k)}\|_2$. Note that the assumption on ρ is a sufficient condition to ensure the convergence, and we observe in practice that a relatively small ρ often yields good performance.

Lemma 2. *(subgradient bound) Under Assumption 1, there exists a vector $\boldsymbol{\eta}^{(k+1)} \in \partial\mathscr{L}\left(\mathbf{u}^{(k+1)}, \mathbf{h}^{(k+1)}, \mathbf{g}^{(k+1)}\right)$ and two constants $c_3, c_4 > 0$ such that*

$$\|\boldsymbol{\eta}^{(k+1)}\|_2^2 \leq c_3\|\mathbf{u}^{(k+1)} - \mathbf{u}^{(k)}\|_2^2 + c_4\|\mathbf{h}^{(k+1)} - \mathbf{h}^{(k)}\|_2^2. \tag{24}$$

Proof. We define

$$\boldsymbol{\eta}_1^{(k+1)} := \frac{\mathbf{p}^{(k+1)}}{\|\mathbf{h}^{(k+1)}\|_2} + A^T\mathbf{w}_1 - \mathbf{w}_2 + \mathbf{w}_3 + \rho D^T\left(D\mathbf{u}^{(k+1)} - \mathbf{h}^{(k+1)} + \mathbf{g}^{(k+1)}\right),$$

where $\mathbf{p}^{(k+1)}$, $\mathbf{w}_1$, $\mathbf{w}_2$, and $\mathbf{w}_3$ are stemmed from (21). Clearly by the subgradient definition, we can prove $A^T\mathbf{w}_1 \in \partial\prod_{A\mathbf{u}=\mathbf{b}}\left(\mathbf{u}^{(k+1)}\right)$ and $\mathbf{w}_3 - \mathbf{w}_2 \in \partial\prod_{[p,q]^N}\left(\mathbf{u}^{(k+1)}\right)$, which implies that $\boldsymbol{\eta}_1^{(k+1)} \in \partial_{\mathbf{u}}\mathscr{L}\left(\mathbf{u}^{(k+1)}, \mathbf{h}^{(k+1)}, \mathbf{g}^{(k+1)}\right)$. Combining the definition of $\boldsymbol{\eta}_1^{(k+1)}$ with (21) leads to

$$\boldsymbol{\eta}_1^{(k+1)} = -\frac{\mathbf{p}^{(k+1)}}{\|\mathbf{h}^{(k)}\|_2} + \frac{\mathbf{p}^{(k+1)}}{\|\mathbf{h}^{(k+1)}\|_2} + \rho D^T\left(\mathbf{h}^{(k)} - \mathbf{h}^{(k+1)}\right) + \rho D^T\left(\mathbf{g}^{(k+1)} - \mathbf{g}^{(k)}\right). \tag{25}$$

To estimate an upper bound of $\|\boldsymbol{\eta}_1^{(k+1)}\|_2$, we apply the chain rule of subgradient, i.e., $\partial\|D\mathbf{u}\|_1 = D^T\mathbf{q}$, where $\mathbf{q} = \{\mathbf{q} | \langle \mathbf{q}, D\mathbf{u}\rangle = \|D\mathbf{u}\|_1, \|\mathbf{q}\|_\infty \le 1\}$, Since $\mathbf{q}^{(k+1)}$ has $2N$ entries, we have $\|\mathbf{p}^{(k+1)}\|_2 \le \|D^T\|_2\|\mathbf{q}^{(k+1)}\|_2 \le 4\sqrt{N}$ based on the facts that $\|\mathbf{x}\|_2 \le \sqrt{l}\|\mathbf{x}\|_\infty, \forall \mathbf{x} \in \mathbb{R}^l$ and $\|D^T\|_2 = \|D\|_2 \le 2\sqrt{2}$. Therefore, we have

$$\left\|\frac{\mathbf{p}^{(k+1)}}{\|\mathbf{h}^{(k+1)}\|_2} - \frac{\mathbf{p}^{(k+1)}}{\|\mathbf{h}^{(k)}\|_2}\right\|_2 \le \frac{1}{\epsilon^2}\|\mathbf{h}^{(k+1)} - \mathbf{h}^{(k)}\|_2\|\mathbf{p}^{(k+1)}\|_2 \le \frac{4\sqrt{N}}{\epsilon^2}\|\mathbf{h}^{(k+1)} - \mathbf{h}^{(k)}\|_2.$$

It further follows from (25) that

$$\|\boldsymbol{\eta}_1^{(k+1)}\|_2 \le \left(\frac{4\sqrt{N}}{\epsilon} + 2\sqrt{2}\rho\right)\|\mathbf{h}^{(k)} - \mathbf{h}^{(k+1)}\|_2 + 2\sqrt{2}\rho\|\mathbf{g}^{(k+1)} - \mathbf{g}^{(k)}\|_2. \quad (26)$$

We can also define $\boldsymbol{\eta}_2^{(k+1)}, \boldsymbol{\eta}_3^{(k+1)}$ such that

$$\boldsymbol{\eta}_2^{(k+1)} \in \nabla_{\mathbf{h}}\mathscr{L}\left(\mathbf{u}^{(k+1)}, \mathbf{h}^{(k+1)}, \mathbf{g}^{(k+1)}\right)$$

$$\boldsymbol{\eta}_3^{(k+1)} \in \nabla_{\mathbf{g}}\mathscr{L}\left(\mathbf{u}^{(k+1)}, \mathbf{h}^{(k+1)}, \mathbf{g}^{(k+1)}\right),$$

and estimate the upper bounds of $\|\boldsymbol{\eta}_2^{(k+1)}\|_2$ and $\|\boldsymbol{\eta}_3^{(k+1)}\|_2$. By denoting $\boldsymbol{\eta}^{(k+1)} = \left(\boldsymbol{\eta}_1^{(k+1)}, \boldsymbol{\eta}_2^{(k+1)}, \boldsymbol{\eta}_3^{(k+1)}\right)$, we have $\boldsymbol{\eta}^{(k+1)} \in \partial\mathscr{L}\left(\mathbf{u}^{(k+1)}, \mathbf{h}^{(k+1)}; \mathbf{g}^{(k+1)}\right)$, and the remaining proof is the same as in [21, Lemma 4.2, Lemma 4.4]. □

Theorem 1. *(subsequential convergence) Under Assumption 1 and a sufficiently large ρ, the sequence* $\{\mathbf{u}^{(k)}, \mathbf{h}^{(k)}, \mathbf{g}^{(k)}\}$ *generated by* (9) *has a subsequence convergent to a stationary point* $(\mathbf{u}^*, \mathbf{h}^*, \mathbf{g}^*)$ *of* $\mathscr{L}$, namely, $\mathbf{0} \in \partial\mathscr{L}(\mathbf{u}^*, \mathbf{h}^*, \mathbf{g}^*)$.

Proof. Since $\mathbf{u}^{(k)} \in [p, q]^N$ is bounded, then $\|D\mathbf{u}^{(k)}\|_1$ is bounded; i.e., there exists a constant $M > 0$ such that $\|D\mathbf{u}^{(k)}\|_1 \le M$. The optimality condition of the $\mathbf{h}$-subproblem in (9) leads to

$$-\frac{a^{(k+1)}}{\|\mathbf{h}^{(k+1)}\|_2^3}\mathbf{h}^{(k+1)} + \rho\left(\mathbf{h}^{(k+1)} - D\mathbf{u}^{(k+1)} - \mathbf{g}^{(k)}\right) = \mathbf{0}, \quad (27)$$

where $a^{(k)} := \|D\mathbf{u}^{(k)}\|_1$. Using the dual update $-\mathbf{g}^{(k+1)} = \mathbf{h}^{(k+1)} - D\mathbf{u}^{(k+1)} - \mathbf{g}^{(k)}$, we have

$$\mathbf{g}^{(k+1)} = -\frac{a^{(k+1)}}{\rho}\frac{\mathbf{h}^{(k+1)}}{\|\mathbf{h}^{(k+1)}\|_2^3}. \quad (28)$$

Due to $\|\mathbf{h}^{(k)}\|_2 \ge \epsilon$ in Assumption 1, we get

$$\|\mathbf{g}^{(k)}\|_2 = \left\| \frac{a^{(k)}}{\rho} \frac{\mathbf{h}^{(k)}}{\|\mathbf{h}^{(k)}\|_2^3} \right\|_2 \le \frac{M}{\rho\epsilon^2},$$

which implies the boundedness of $\{\mathbf{g}^{(k)}\}$. It follows from the $\mathbf{h}$-update (10) that $\{\mathbf{h}^{(k)}\}$ is also bounded. Therefore, the Bolzano-Weierstrass Theorem guarantees that the sequence $\{\mathbf{u}^{(k)}, \mathbf{h}^{(k)}, \mathbf{g}^{(k)}\}$ has a convergent subsequence, denoted by $\left(\mathbf{u}^{(k_j)}, \mathbf{h}^{(k_j)}, \mathbf{g}^{(k_j)}\right) \to \left(\mathbf{u}^*, \mathbf{h}^*, \mathbf{g}^*\right)$, as $k_j \to \infty$. In addition, we can estimate that

$$\begin{aligned}
&\mathscr{L}\left(\mathbf{u}^{(k)}, \mathbf{h}^{(k)}; \mathbf{g}^{(k)}\right) \\
&= \frac{\|D\mathbf{u}^{(k)}\|_1}{\|\mathbf{h}^{(k)}\|_2} + \prod_{A\mathbf{u} = \mathbf{b}}\left(\mathbf{u}^{(k)}\right) + \prod_{[p,q]^N}\left(\mathbf{u}^{(k)}\right) + \frac{\rho}{2}\|\mathbf{h}^{(k)} - D\mathbf{u}^{(k)} - \mathbf{g}^{(k)}\|_2^2 - \frac{\rho}{2}\|\mathbf{g}^{(k)}\|_2^2 \\
&\ge \frac{\|D\mathbf{u}^{(k)}\|_1}{\|\mathbf{h}^{(k)}\|_2} - \frac{M^2}{2\rho\epsilon^4},
\end{aligned}$$

which gives a lower bound of $\mathscr{L}$ owing to the boundedness of $\mathbf{u}^{(k)}$ and $\mathbf{h}^{(k)}$. It further follows from Lemma 1 that $\mathscr{L}\left(\mathbf{u}^{(k)}, \mathbf{h}^{(k)}, \mathbf{g}^{(k)}\right)$ converges due to its monotonicity.

We then sum the inequality (18) from $k = 0$ to K, thus getting

$$\begin{aligned}
&\mathscr{L}\left(\mathbf{u}^{(K+1)}, \mathbf{h}^{(K+1)}; \mathbf{g}^{(K+1)}\right) \\
&\le \mathscr{L}\left(\mathbf{u}^{(0)}, \mathbf{h}^{(0)}; \mathbf{g}^{(0)}\right) - c_1 \sum_{k=0}^{K} \|\mathbf{u}^{(k+1)} - \mathbf{u}^{(k)}\|_2^2 - c_2 \sum_{k=0}^{K} \|\mathbf{h}^{(k+1)} - \mathbf{h}^{(k)}\|_2^2.
\end{aligned}$$

Let $K \to \infty$, we have both summations of $\sum_{k=0}^{\infty} \|\mathbf{u}^{(k+1)} - \mathbf{u}^{(k)}\|_2^2$ and $\sum_{k=0}^{\infty} \|\mathbf{h}^{(k+1)} - \mathbf{h}^{(k)}\|_2^2$ are finite, indicating that $\mathbf{u}^{(k)} - \mathbf{u}^{(k+1)} \to 0$, $\mathbf{h}^{(k)} - \mathbf{h}^{(k+1)} \to 0$. Then by [21, Lemma 4.2], we get $\mathbf{g}^{(k)} - \mathbf{g}^{(k+1)} \to 0$. By $\left(\mathbf{u}^{(k_j)}, \mathbf{h}^{(k_j)}, \mathbf{g}^{(k_j)}\right) \to \left(\mathbf{u}^*, \mathbf{h}^*, \mathbf{g}^*\right)$, we have $\left(\mathbf{u}^{(k_j+1)}, \mathbf{h}^{(k_j+1)}, \mathbf{g}^{(k_j+1)}\right) \to \left(\mathbf{u}^*, \mathbf{h}^*, \mathbf{g}^*\right)$, $A\mathbf{u}^* = \mathbf{b}$ (as $A\mathbf{u}^{(k_j)} = \mathbf{b}$), and $D\mathbf{u}^* = \mathbf{h}^*$ (by the update of $\mathbf{g}$). It further follows from Lemma 2 that $\mathbf{0} \in \partial L\left(\mathbf{u}^*, \mathbf{h}^*, \mathbf{g}^*\right)$ and hence $(\mathbf{u}^*, \mathbf{h}^*, \mathbf{g}^*)$ is a stationary point of (8). □

Lastly, we establish the global convergence, i.e., the entire sequence converges, which is stronger than the subsequential convergence as in Theorem 1. In particular, we show in Lemma 3 that the modified Lagrangian $\mathscr{L}_\epsilon$ defined in (17) has the Kurdyka-Łojasiewicz (KL) property [26]; see Definition 1. The global convergence of the proposed scheme (9) is characterized in Theorem 2, which can be proven in a similar way as [27, Theorem 4].

Definition 1. *(KL property* [26]) *We say a proper closed function* $h: \mathbb{R}^n \to (-\infty, +\infty]$ *satisfies the KL property at a point* $\hat{\mathbf{x}} \in \mathrm{dom}\,\partial h$ *if there exist a constant* $\nu \in (0, \infty]$, *a neighborhood U of* $\hat{\mathbf{x}}$, *and a continuous concave function* $\phi: [0, \nu) \to [0, \infty)$ *with* $\phi(0) = 0$ *such that*

i. *ϕ is continuously differentiable on* $(0, \nu)$ *with* $\phi' > 0$ *on* $(0, \nu)$;

ii. *for every* $\mathbf{x} \in U$ *with* $h(\hat{\mathbf{x}}) < h(\mathbf{x}) < h(\hat{\mathbf{x}}) + \nu$, *it holds that*

$$\phi'(h(\mathbf{x}) - h(\hat{\mathbf{x}}))\mathrm{dist}(\mathbf{0}, \partial h(\mathbf{x})) \geq 1,$$

where $\mathrm{dist}(\mathbf{x}, C)$ *denotes the distance from a point* $\mathbf{x}$ *to a closed set* C *measured in* $\|\cdot\|_2$ *with a convention of* $\mathrm{dist}(\mathbf{0}, \emptyset) := +\infty$.

Lemma 3. $\mathscr{L}_\epsilon$ *defined in* (17) *satisfies the KL property.*

Proof. Specifically, we show that $\mathscr{L}_\epsilon$ in (17) is semialgebraic by definition. Indeed, note that the graph of $\mathscr{L}_\epsilon$ can be written as

$$\begin{aligned}
\mathrm{gph}(\mathscr{L}_\epsilon) &= \left\{ (\mathbf{u}, \mathbf{h}, \mathbf{g}, t) \left| \begin{array}{c} t = \dfrac{\|D\mathbf{u}\|_1}{\|\mathbf{h}\|_2} + \langle \rho \mathbf{g}, D\mathbf{u} - \mathbf{h} \rangle + \dfrac{\rho}{2}\|D\mathbf{u} - \mathbf{h}\|_2^2, \quad \mathbf{u} \in [p, q]^N, \\ A\mathbf{u} = \mathbf{b}, \quad \|\mathbf{h}\|_2 \geq \epsilon/2 \end{array} \right. \right\} \\
&= \left\{ (\mathbf{u}, \mathbf{h}, \mathbf{g}, t) \left| \begin{array}{c} t = w + \langle \rho \mathbf{g}, D\mathbf{u} - \mathbf{h} \rangle + \dfrac{\rho}{2}\|D\mathbf{u} - \mathbf{h}\|_2^2, \\ \mathbf{u} \in [p, q]^N, A\mathbf{u} = \mathbf{b}, \quad \|\mathbf{h}\|_2 \geq \epsilon/2, \quad \|D\mathbf{u}\|_1 = w\|\mathbf{h}\|_2 \end{array} \right. \right\} \\
&= \left\{ (\mathbf{u}, \mathbf{h}, \mathbf{g}, t) \left| \begin{array}{c} t = w + \langle \rho \mathbf{g}, D\mathbf{u} - \mathbf{h} \rangle + \dfrac{\rho}{2}\|D\mathbf{u} - \mathbf{h}\|_2^2, \\ \mathbf{u} \in [p, q]^N, A\mathbf{u} = \mathbf{b}, \quad \|\mathbf{h}\|_2^2 \geq (\epsilon/2)^2, \quad \|D\mathbf{u}\|_1^2 = w^2\|\mathbf{h}\|_2^2, \quad w \geq 0 \end{array} \right. \right\}.
\end{aligned}$$

This implies that $\mathrm{gph}(\mathscr{L}_\epsilon)$ can be written as a finite union and intersection of level sets of polynomials, meaning that $\mathscr{L}_\epsilon$ is semialgebraic. Since $\mathscr{L}_\epsilon$ is also proper and closed, it satisfies the KL property; see, for example, [28, Section 4.3]. □

Theorem 2. *(global convergence) Under the Assumption 1 and a sufficiently large ρ, the sequence* $\{\mathbf{u}^{(k)}, \mathbf{h}^{(k)}, \mathbf{g}^{(k)}\}$ *generated by* (9) *converges to a stationary point of* (8).

Proof. It is straightforward that $\mathscr{L}_\epsilon$ is subdifferentiable with respect to $\mathbf{u}$ and continuously differentiable with respect to $\mathbf{h}$ for $\|\mathbf{h}\|_2 \geq \epsilon$. The global convergence follows almost the same as [27, Theorem 4], which does not require any specific form of $\mathscr{L}$, and hence we omit the rest of the proof. □

5. Experimental results

In this section, we test the proposed algorithm on three prototypical imaging applications: super-resolution, MRI reconstruction, and limited-angle CT reconstruction. Here super-resolution refers to recovering a 2D image from low-frequency measurements, i.e., we restrict the data within a square in the center of the frequency domain; please refer to Section 6 for the definition of 1D super-resolution. The data measurements for the MRI reconstruction are taken along radial lines in the frequency domain; such a radial pattern [29] is referred to as a mask. The sensing matrix for the CT reconstruction is the Radon transform [30], while the term “limited-angle” means the rotating angle does not cover the entire circle [31, 32, 33].

We evaluate the performance in terms of the relative error (RE) and the peak signal-to-noise ratio (PSNR), defined by

$$\mathrm{RE}(\mathbf{u}^*, \tilde{\mathbf{u}}) := \frac{\|\mathbf{u}^* - \tilde{\mathbf{u}}\|}{\|\tilde{\mathbf{u}}\|_2} \quad \text{and} \quad \mathrm{PSNR}(\mathbf{u}^*, \tilde{\mathbf{u}}) := 10\log_{10}\frac{NP^2}{\|\mathbf{u}^* - \tilde{\mathbf{u}}\|_2^2},$$

where $\mathbf{u}^*$ is the restored image, $\tilde{\mathbf{u}}$ is the ground truth, and P is the maximum peak value of $\tilde{\mathbf{u}}$.

To ease the parameter tuning, we scale the pixel value to [0, 1] for the original images in each application and rescale the solution back after computation. Hence the box constraint is set as [0, 1]. We start by discussing some algorithmic behaviors regarding the box constraint, the maximum number of inner iterations, and sensitivity analysis on algorithmic parameters in Section 5.1. The remaining sections are organized by specific applications. We compare the proposed L_1/L_2 approach with total variation (L_1 on the gradient) [1] and two nonconvex regularizations: L_p for $p = 0.5$ and L_1-αL_2 ($\alpha = 0.5$ as suggested in [34]) on the gradient. To solve for the L_p model, we replace the soft shrinkage (16) by the proximal operator corresponding to L_p that was derived in [35], and apply the same ADMM framework as the L_1 minimization. To have a fair comparison, we incorporate the [0, 1] box constraint in L_1, L_p, L_1-αL_2, and L_1/L_2 models. We implement all these competing methods by ourselves and tune the parameters to achieve the smallest RE to the ground-truth. Due to the constrained formulation, no noise is added. We set the initial condition of $\mathbf{u}$ to be a zero vector for all the methods. The stopping criterion for the proposed Algorithm 1 is when the relative error between two consecutive iterates is smaller than $\epsilon = 10^{-5}$ for both inner and outer iterations. All the numerical experiments are carried out in a desktop with CPU (Intel i7–9700F, 3.00 GHz) and MATLAB 9.8 (R2020a).

5.1. Algorithmic behaviors

We discuss three computational aspects of the proposed Algorithm 1. In particular, we want to analyze the influence of the box constraint, the maximum number of inner iterations (denoted by jMax), and the algorithmic parameters on the reconstruction results of MRI and CT problems. We use MATLAB’s built-in function phantom, which is called the Shepp-Logan (SL) phantom, to test on 6 radial lines for MRI and 45° scanning range for CT. The analysis is assessed in terms of objective values $\frac{\|D\mathbf{u}^{(k)}\|_1}{\|D\mathbf{u}^{(k)}\|_2}$ and $\mathrm{RE}\left(\mathbf{u}^{(k)}, \tilde{\mathbf{u}}\right)$ versus the CPU time.

In Figure 1, we present algorithmic behaviors of the box constraint for both MRI and CT problems, in which we set jMax to be 5 and 1, respectively (we will discuss the effects of inner iteration number shortly.) In the MRI problem, the box constraint is critical; without it, our algorithm converges to another local minimizer, as RE goes up. With the box constraint, the objective values decrease faster than in the no-box case, and the relative errors drop down monotonically. In the CT case, the influence of box is minor but we can see a faster decay of RE than the no-box case after 200 seconds. In the light of these observations, we only consider the algorithm with a box constraint for the rest of the experiments.

We then study the effect of jMax on MRI/CT reconstruction problems in Figure 2. We fix the maximum outer iterations as 300, and examine four possible jMax values: 1, 3, 5 and 10. In the case of MRI, jMax = 10 causes the slowest decay of both objective value and RE. Besides, we observe that only one inner iteration, which is equivalent to our previous approach [18], is not as efficient as more inner iterations to reduce the RE in the MRI problem. The CT results are slightly different, as one inner iteration seems sufficient to yield satisfactory results. The disparate behavior of CT to MRI is probably due to inexact solutions by CG iterations. In other words, more inner iterations do not improve the accuracy. Following Figure 2, we set jMax to be 5 and 1 in MRI and CT, respectively, for the rest of the experiments.

Lastly, we study the sensitivity of the parameters λ, ρ, β in our proposed algorithm to provide strategies for parameter selection. For simplicity, we set $\gamma = \rho$ as their corresponding auxiliary variables represent $D\mathbf{u}$. In the MRI reconstruction problem, we examine three values of $\lambda \in \{100, 1000, 10000\}$ and two settings of the number of maximum outer iterations, i.e., kMax $\in \{500, 1000\}$. For each combination of λ and kMax, we vary parameters $(\rho, \beta) \in (2^i, 2^j)$, for $i, j \in [-4, 4]$, and plot the RE in Figure 3. We observe that small values of ρ work well in practice, although we need to assume a sufficiently large value for ρ when proving the convergence results in Theorems 1 and 2. Besides, a larger kMax value leads to larger valley regions for the lowest RE, which verifies that only ρ and β affect the convergence rate. Figure 3 suggests that our algorithm is generally insensitive to β, ρ and λ, as long as ρ is small. Similarly in the CT reconstruction, we set $\lambda \in \{0.005, 0.05, 0.5\}$, kMax $\in \{100, 300\}$, and $(\rho, \beta) \in (2^i, 2^j)$, for $i, j \in [-4, 4]$. Figure 4 shows that ρ and β can be selected in a wide range, especially for large number of outer iterations. But our algorithm is sensitive to λ for the CT problem, as $\lambda = 0.005$ or 0.5 yields larger errors than $\lambda = 0.05$. In the light of this sensitivity analysis, we can tune parameters by finding the optimal combination among a candidate set for each problem, paying specific attention to the value of λ in the limited-angle CT reconstruction.

5.2. Super-resolution

We use an original image from [36] of size 688×688 to illustrate the performance of super-resolution. As super-resolution is similar to MRI in the sense of frequency measurements, we set up the maximum iteration number as 5 according to Section 5.1. We restrict the data within a square in the center of the frequency domain (corresponding to low-frequency measurements), and hence varying the sizes of the square leads to different sampling ratios. In addition to regularized methods, we include a direct method of filling in the unknown frequency data by zero, followed by inverse Fourier transform, which is referred to as zero-filling (ZF). The visual results of 1% are presented in Figure 5, showing that both L_p and L_1/L_2 are superior over ZF, L_1, and L_1-αL_2. Specifically, L_1/L_2 can recover these thin rectangular bars, while L_1 and L_1-αL_2 lead to thicker bars with white background, which should be gray. In addition, L_p and L_1/L_2 can recover the most of the letter ‘a’ in the bottom of the image, compared to the other methods, while L_1/L_2 is better than L_p with more natural boundaries along the six dots in the middle left of the image. One drawback of L_1/L_2 is that it produces white artifacts near the third square from the left as well as around the letter 'a' in the middle. We suspect L_1/L_2 is not very stable, and the box constraint forces the black-and-white regions near edges. We do not present quantitative measures for this example, as four noisy squares on the right of the image lead to meaningless comparison, considering that all the methods return smooth results.

5.3. MRI reconstruction

To generate the ground-truth MRI images, we utilize a simulated brain database [37, 38] that has full three-dimensional data volumes obtained by an MRI simulator [39] in different modalities such as T1 and T2 weighted images. As a proof of concept, we extract one slice from the 3D T1 and T2 data as testing images and take frequency data along radial lines. The visual comparisons are presented for 25 radial lines (about 13.74% measurements) in Figure 6. We include the zero-filled method as mentioned in super-resolution, which unfortunately fails to recover the contrast for both T1 and T2. The other regularization methods yield more blurred results than the proposed L_1/L_2 approach. Particularly worth noticing is that our proposed model can effectively separate the gray matter and white matter in the T1 image, as highlighted in the zoom-in regions. Furthermore, we plot the horizontal and vertical profiles in Figure 7, where we can see clearly that the restored profiles via L_1/L_2 are closer to the ground truth than the other approaches, especially near these peaks that can be reached by L_p, L_1-αL_2, and L_1/L_2, but not L_1. As a further comparison, we present the MRI reconstruction results under various number of lines (20, 25, and 30) in Table 1, which demonstrates significant improvements of L_1/L_2 over the other models in term of PSNR and RE.

5.4. Limited-angle CT reconstruction

Lastly, we examine the limited-angle CT reconstruction problem on two standard phantoms: Shepp-Logan (SL) by Matlab's built-in command (phantom) and FORBILD (FB) [40]. Notice that the FB phantom has a very low image contrast and we display it with the grayscale window of [1.0, 1.2] in order to reveal its structures; see Figure 8. To synthesize the CT projected data, we discretize both phantoms at a resolution of 256 × 256. The forward operator A is generated as the discrete Radon transform with a parallel beam geometry sampled at $\theta_{\text{Max}}/30$ over a range of θ_{Max}, resulting in a sub-sampled data of size 362 × 31. Note that we use the same number of projections when we vary ranges of projection angles. The simulation process is available in the IR and AIR toolbox [41, 42]. Following the discussion in Section 5.1, we set jMax = 1 for the subproblem. We compare the regularization models with a clinical standard approach, called simultaneous algebraic reconstruction technique (SART) [43].

As the SL phantom has relatively simpler structures than FB, we present an extremely limited angle of only 30° scanning range in Table 2, which shows that L_1/L_2 achieves significant improvements over SART, L_1, L_p, and L_1-αL_2 in terms of PSNR and RE. Visually, we present the CT reconstruction results of 45° projection range for SL (SL-45°) and 75° for FB (FB-75°) in Figure 8. In the first case (SL-45°), SART fails to recover the ellipse inside of the skull with such a small range of projection angles. All the modern regularization methods perform much better than SART owing to their sparsity promoting property. However, the L_1 model is unable to restore the bottom skull and preserve details of some ellipses in the middle. The proposed L_1/L_2 method leads an almost exact recovery with a relative error of 0.64% and visually no difference to the ground truth. In the second case (FB-75°), we show the reconstructed images with the window of [1.0, 1.2], and observe some fluctuations inside of the skull. L_p performs the best, while L_1/L_2 restores the most details of the image among the competing methods. We plot the horizontal and vertical profiles in Figure 9, which illustrates that L_1/L_2 leads to the smallest fluctuations compared to the other methods. We also observe a well-known artifact of the L_1 method, i.e., loss-of-contrast, as its profile fails to reach the height of jump on the intervals such as [160, 180] in the left plot and [220, 230] in the right plot of Figure 9, while L_1/L_2 has a good recovery in these regions.

6. Empirical studies

We aim to empirically demonstrate the superiority of L_1/L_2 on the gradient over TV based on a super-resolution problem [44], in which a sparse vector can be exactly recovered via the L_1 minimization. *Super-resolution* refers to recovering a sparse signal from its low-frequency measurements, which can be expressed mathematically as

$$b_k = \frac{1}{\sqrt{N}} \sum_{j=0}^{N-1} u_j e^{-i2\pi kj/N}, \qquad |k| \le f_c, \tag{29}$$

where i is the imaginary unit, $\mathbf{u} \in \mathbb{R}^N$ is a vector to be recovered, and $\mathbf{b} \in \mathbb{C}^n$ consists of the given low frequency measurements with $n = 2f_c + 1 < N$. Recovering $\mathbf{u}$ from $\mathbf{b}$ is referred to as super-resolution in the sense that the underlying signal $\mathbf{u}$ is defined on a fine grid with spacing $1/N$, while a direct inversion of n frequency data yields a signal defined on a coarser grid with spacing $1/n$. For simplicity, we use matrix notation to rewrite (29) as $\mathbf{b} = S_n F \mathbf{u}$, where S_n is a sampling matrix that collects the required low frequencies and F is the Fourier transform matrix.

A sparse signal can be represented by $\mathbf{u} = \sum_{j \in T} c_j \mathbf{e}_j$, where $\mathbf{e}_j$ is the j-th canonical basis in $\mathbb{R}^N$, T is the support set of $\mathbf{u}$, and $\{c_j\}$ are coefficients. Candés and Fernandez-Granda [45] proved that if a signal has spikes (locations of nonzero elements) that are sufficiently separated, then the L_1 minimization yields an exact recovery for super-resolution. To make the paper self-contained, we provide the definition of minimum separation in Definition 2 and an exact recovery condition in Theorem 3.

Definition 2. *(Minimum Separation* [44]) *For an index set* $T \subset \{1, \cdots, N\}$, *the minimum separation (MS) of T is defined as the closest wrap-around distance between any two elements from T,*

$$\Delta(T) := \min_{(t,\tau) \in T : t \ne \tau} \min\{|t - \tau|, N - |t - \tau|\}. \tag{30}$$

Theorem 3. [44, *Corollary 1.4] Let T be the support of* **u**. *If the minimum separation of T obeys*

$$\Delta(T) \geq \frac{1.87N}{f_c}, \tag{31}$$

then $\mathbf{u} \in \mathbb{R}^N$ *is the unique solution to the constrained* L_1 *minimization problem,*

$$\min_{\mathbf{u}} \|\mathbf{u}\|_1 \quad \text{s.t.} \quad S_n F\mathbf{u} = \mathbf{b}. \tag{32}$$

We extend the analysis from sparse signals to sparse gradients for two purposes. On one hand, this empirical study reveals a hypothesis that the TV minimization can find the desired solution under a similar separation condition as in [45]. On the other hand, we illustrate that L_1/L_2 can deal with less separated spikes in gradient, and is better at preserving image contrast than L_1. These empirical evidences show L_1/L_2 holds great potentials in promoting sparse gradients and preserving image contrasts. To the best of our knowledge, it is the first time to relate the exact recovery of gradient-based methods to minimum separation and image contrast in a super-resolution problem. Prior works [**?**, **?**, **?**, **?**] on TV exact recovery are mostly about the sampling matrix, i.e., S_n, while we focus on the ground-truth image.

We design a certain type of piecewise constant signals that lead to well-separated spikes after taking the gradient. In particular, we construct a one-bar step function of length 100 with the first and the last s elements taking value 0, and the remaining elements equal to 1, as illustrated in Figure 10. The gradient of such signal is 2-sparse with MS to be min(2s, 100 − 2s) due to wrap-around distance. By setting $f_c = 2$, we only take $n = 5$ low frequency measurements, and reconstruct the signal by minimizing either L_1 or L_1/L_2 on the gradient. For simplicity, we adopt the CVX MATLAB toolbox [46] for solving the TV model,

$$\min_{\mathbf{u}} \|D\mathbf{u}\|_1 \quad \text{s.t.} \quad A\mathbf{u} = \mathbf{b}, \tag{33}$$

where we use $A = S_n F$ to be consistent with our setting (2). Please refer to Section 3 for more details on the L_1/L_2 minimization, in which one subproblem can be solved by CVX rather than ADMM with a need to tune the parameter ρ.

By varying the value of s that changes MS of the spikes in gradient, we compute the relative errors between the reconstructed solutions and the ground-truth signals.

If we define an exact recovery for its relative error smaller than 10^{-6}, we observe in Figure 10 that the exact recovery by L_1 occurs at $s \in [13, 37]$, which implies that MS is larger than or equal to 26. This phenomenon suggests that Theorem 3 might hold for sparse gradients by replacing the L_1 norm with the total variation. Figure 10 also shows the exact recovery by L_1/L_2 at $s \in [12, 38]$, meaning that L_1/L_2 can deal with less separated spikes than L_1. Moreover, we further study the reconstruction results at $s = 39$, where both models fail to find the true sparse signal. The restored solutions by these two models as well as the different plots between restored and ground truth are displayed in Figure 11, showing that L_1/L_2 has smaller relative errors than L_1.

Figure 11 illustrates that the TV solution can not reach the top of the bar in the ground-truth, which is referred to as *loss-of-contrast*. Motivated by this well-known drawback of TV, we postulate that the signal contrast may affect the performance of L_1 and L_1/L_2. To verify, we examine a two-bar step function, in which the contrast varies by the relative heights of the two bars. Following MATLAB's notation, we set $\mathbf{u}(s+1:2s)=2$, $\mathbf{u}(\text{end}-2s+1:\text{end})=1$, and the value of remaining elements uniformly as t; see Figure 12 for a general setting. We fix $s=12$, and vary the value of $t\in(1,2)$ to generate signals with different intensity contrasts. Considering four spikes in the gradient, we set $f_c=4$ or equivalently 9 low-frequency measurements to reconstruct the signal. The reconstruction errors are plotted in Figure 12, which shows that L_1 fails in all the cases, and L_1/L_2 can recover the signals except for $t\in[1.5, 1.65]$. We further examine a particular case of $t=1.65$ in Figure 13, where both models fail to get an exact recovery, but L_1/L_2 yields smaller oscillations than L_1 near the edges. Figures 12 and 13 demonstrate L_1/L_2 is better at preserving image contrast than L_1.

We verify that all the solutions of L_1 and L_1/L_2 satisfy the linear constraint $A\mathbf{u}=\mathbf{b}$ with high accuracy thanks for CVX. We further investigate when the L_1 approach fails, discovering that it yields a solution that has a smaller L_1 norm compared to the L_1 norm of the ground-truth, which implies that L_1 is not sufficient to enforce gradient sparse. On the other hand, L_1/L_2 solutions often have higher objective value than the ground-truth, which calls for a better algorithm that can potentially find the ground-truth. We also want to point out that L_1/L_2 solutions depend on initial conditions. In Figure 10 and Figure 12, we present the smallest relative errors among 10 random vectors for initial values.

The minimum separation distance in 1D (Definition 2) can be naturally extended to 2D. In fact, there are two types of minimum separation definitions in 2D: one uses the L_∞ norm to measure the distance [44], while another definition is called *Rayleigh regularity* [47, 48]. The exact recovery for 2D sparse vectors was characterized in [48] with additional restriction of positive signals. Both distance definitions were empirically examined in [12] for point-source super-resolution. When extending to 2D sparse gradient, one can compute the gradient norm at each pixel, and separation distance can be defined as the distance between any two locations with non-zero gradient norm. To the best of our knowledge, there is no analysis on the exact recovery of sparse gradients, no matter whether it is in 1D or 2D, which calls for a theoretical justification in the future. Once the extension from 1D sparse vectors to 1D sparse gradients is established, it is expected that the analysis can be applied to sparse gradients in 2D to facilitate theoretical analysis in imaging applications.

7. Conclusions and future works

In this paper, we considered the use of L_1/L_2 on the gradient as an objective function to promote sparse gradients for imaging problems. We proposed a splitting algorithm scheme of minimizing a constrained model that has provable convergence for ADMM. We conducted extensive experiments to demonstrate that our approach outperforms the state-of-the-art gradient-based approaches. We provided some empirical evidences on the superiority of the ratio model over L_1, which may motivate future studies on the exact recovery of the TV regularization with respect to the minimum separation of the gradient spikes. We are also interested in extending the analysis to the unconstrained formulation, which is widely applicable in image processing.

Acknowledgments

C. Wang was partially supported by HKRGC Grant No.CityU11301120 and NSF CCF HDR TRIPODS grant 1934568. M. Tao was supported in part by the Natural Science Foundation of China (No. 11971228) and the Jiangsu Provincial National Natural Science Foundation of China (No. BK20181257). C-N. Chuah was partially supported by Child Family Endowed Professorship. J. Nagy was partially supported by NSF DMS-1819042 and NIH 5R01CA181171–04. Y. Lou was partially supported by NSF grant CAREER 1846690. All the authors would like to acknowledge Dr. Ting Kei Pong from the Hong Kong Polytechnic University for his clarification on the KL property and global convergence.

References

[1]. Rudin L, Osher S, Fatemi E. Nonlinear total variation based noise removal algorithms. Physica D 1992;60:259–268.

[2]. Bredies K, Kunisch K, Pock T. Total generalized variation. SIAM J Imaging Sci 2010;3(3):492–526.

[3]. Chen D, Chen YQ, Xue D. Fractional-order total variation image denoising based on proximity algorithm. Appl Math Comput 2015;257(1):537–545.

[4]. Zhang J, Chen K. A total fractional-Order variation model for image restoration with nonhomogeneous boundary conditions and its numerical solution. SIAM J Imaging Sci 2015;8(4):2487–2518.

[5]. Osher SJ, Esedoglu S. Decomposition of images by the anisotropic Rudin-Osher-Fatemi model. Comm Pure Appl Math 2003;57:1609–1626.

[6]. Natarajan BK. Sparse approximate solutions to linear systems. SIAM J Comput 1995;p. 227–234.

[7]. Candès EJ, Romberg J, Tao T. Stable signal recovery from incomplete and inaccurate measurements. Comm Pure Appl Math 2006;59:1207–1223.

[8]. Fan J, Li R. Variable selection via nonconcave penalized likelihood and its oracle properties. J Am Stat Assoc 2001;96(456):1348–1360.

[9]. Zhang C Nearly unbiased variable selection under minimax concave penalty. Ann Stat 2010;p. 894–942.

[10]. Zhang T Multi-stage convex relaxation for learning with sparse regularization. In: Adv. Neural. Inf. Process. Syst; 2009. p. 1929–1936.

[11]. Shen X, Pan W, Zhu Y. Likelihood-based selection and sharp parameter estimation. J Am Stat Assoc 2012;107(497):223–232. [PubMed: 22736876]

[12]. Lou Y, Yin P, Xin J. Point source super-resolution via non-convex L1 based methods. J Sci Comput 2016;68:1082–1100.

[13]. Lv J, Fan Y. A unified approach to model selection and sparse recovery using regularized least squares. Ann Appl Stat 2009;p. 3498–3528.

[14]. Zhang S, Xin J. Minimization of transformed L1 penalty: closed form representation and iterative yhresholding algorithms. Comm Math Sci 2017;15:511–537.

[15]. Zhang S, Xin J. Minimization of transformed L1 penalty: theory, difference of convex function algorithm, and robust application in compressed sensing. Math Program 2018;169:307–336.

[16]. Chartrand R Exact reconstruction of sparse signals via nonconvex minimization. IEEE Signal Process Lett 2007;10(14):707–710.

[17]. You J, Jiao Y, Lu X, Zeng T. A nonconvex model with minimax concave penalty for image restoration. J Sci Comput 2019;78(2):1063–1086.

[18]. Rahimi Y, Wang C, Dong H, Lou Y. A scale invariant approach for sparse signal recovery. SIAM J Sci Comput 2019;41(6):A3649–A3672.

[19]. Wang C, Yan M, Rahimi Y, Lou Y. Accelerated schemes for the L1/L2 minimization. IEEE Trans Signal Process 2020;68:2660–2669.

[20]. Tao M Minimization of L1 over L2 for sparse signal recovery with convergence guarantee; 2020. http://www.optimization-online.org/DB_HTML/2020/10/8064.html.

[21]. Wang C, Tao M, Nagy J, Lou Y. Limited-angle CT reconstruction via the L1/L2 minimization. SIAM J Imaging Sci 2021;14(2):749–777.

[22]. Boyd S, Parikh N, Chu E, Peleato B, Eckstein J. Distributed optimization and statistical learning via the alternating direction method of multipliers. Found Trends Mach Learn 2011 Jan;3(1):1–122.

[23]. Chan RH, Ma J. A multiplicative iterative algorithm for box-constrained penalized likelihood image restoration. IEEE Trans Image Process 2012;21(7):3168–3181. [PubMed: 22374363]

[24]. Kan K, Fung SW, Ruthotto L. PNKH-B: A Projected Newton-Krylov Method for Large-Scale Bound-Constrained Optimization. arXiv preprint arXiv:200513639.2020;.

[25]. Nocedal J, Wright SJ. Numerical Optimization Springer; 2006.

[26]. Bolte J, Daniilidis A, Lewis A. The Lojasiewicz inequality for nonsmooth subanalytic functions with applications to subgradient dynamical systems. SIAM J Optim 2007;17(4):1205–1223.

[27]. Li G, Pong TK. Global convergence of splitting methods for nonconvex composite optimization. SIAM J Optim 2015;25(4):2434–2460.

[28]. Attouch H, Bolte J, Redont P, Soubeyran A. Proximal alternating minimization and projection methods for nonconvex problems: An approach based on the Kurdyka-Łojasiewicz inequality. Mathematics of operations research 2010;35(2):438–457.

[29]. Candès EJ, Romberg J, Tao T. Robust uncertainty principles: Exact signal reconstruction from highly incomplete frequency information. IEEE Trans Inf Theory 2006;52(2):489–509.

[30]. Avinash C, Malcolm S. Principles of computerized tomographic imaging Philadelphia, PA, USA: Society for Industrial and Applied Mathematics; 2001.

[31]. Chen Z, Jin X, Li L, Wang G. A limited-angle CT reconstruction method based on anisotropic TV minimization. Phys Med Biol 2013;58(7):2119. [PubMed: 23470430]

[32]. Zhang Y, Chan HP, Sahiner B, Wei J, Goodsitt MM, Hadjiiski LM, et al. A comparative study of limited-angle cone-beam reconstruction methods for breast tomosynthesis. Med Phys 2006;33(10):3781–3795. [PubMed: 17089843]

[33]. Wang Z, Huang Z, Chen Z, Zhang L, Jiang X, Kang K, et al. Low-dose multiple-information retrieval algorithm for X-ray grating-based imaging. Nucl Instrum Methods Phys 2011;635(1):103–107.

[34]. Lou Y, Zeng T, Osher S, Xin J. A weighted difference of anisotropic and isotropic total variation model for image processing. SIAM J Imaging Sci 2015;8(3):1798–1823.

[35]. Xu Z, Chang X, Xu F, Zhang H. $L_{1/2}$ Regularization: A Thresholding Representation Theory and a Fast Solver. IEEE Trans Neural Netw Learn Syst 2012;23:1013–1027. [PubMed: 24807129]

[36]. Gonzalez RC, Woods RE, Eddins SL. Digital image processing using MATLAB Pearson Education India; 2004.

[37]. Cocosco CA, Kollokian V, Kwan RKS, Pike GB, Evans AC. BrainWeb: Online Interface to a 3D MRI Simulated Brain Database. NeuroImage 1997;5:425.

[38]. Kwan RS, Evans AC, Pike GB. MRI simulation-based evaluation of image-processing and classification methods. IEEE Trans Med Imaging 1999;18(11):1085–1097. [PubMed: 10661326]

[39]. Kwan RKS, Evans AC, Pike GB. An extensible MRI simulator for post-processing evaluation. In: International Conference on Visualization in Biomedical Computing Springer; 1996. p. 135–140.

[40]. Yu Z, Noo F, Dennerlein F, Wunderlich A, Lauritsch G, Hornegger J. Simulation tools for two-dimensional experiments in x-ray computed tomography using the FORBILD head phantom. Phys Med Biol 2012;57(13):N237. [PubMed: 22713335]

[41]. Gazzola S, Hansen PC, Nagy JG. IR Tools: a MATLAB package of iterative regularization methods and large-scale test problems. Numer Algorithms 2019;81(3):773–811.

[42]. Hansen PC, Saxild-Hansen M. AIR tools — MATLAB package of algebraic iterative reconstruction methods. J Comput Appl Math 2012;236(8):2167–2178.

[43]. Andersen AH, Kak AC. Simultaneous algebraic reconstruction technique (SART): a superior implementation of the ART algorithm. Ultrason Imaging 1984;6(1):81–94. [PubMed: 6548059]

[44]. Candès EJ, Fernandez-Granda C. Towards a mathematical theory of super-resolution. Comm Pure Appl Math 2014;67(6):906–956.

[45]. Candès EJ, Fernandez-Granda C. Super-resolution from noisy data. J Fourier Anal Appl 2013;19(6):1229–1254.

[46]. Grant M, Boyd S. CVX: Matlab Software for Disciplined Convex Programming, version 2.1; 2014. http://cvxr.com/cvx.

[47]. Donoho DL. Superresolution via sparsity constraints. SIAM J Math Anal 1992;23(5):1309–1331.

[48]. Morgenshtern VI, Candes EJ. Super-resolution of positive sources: The discrete setup. SIAM Journal on Imaging Sciences 2016;9(1):412–444.

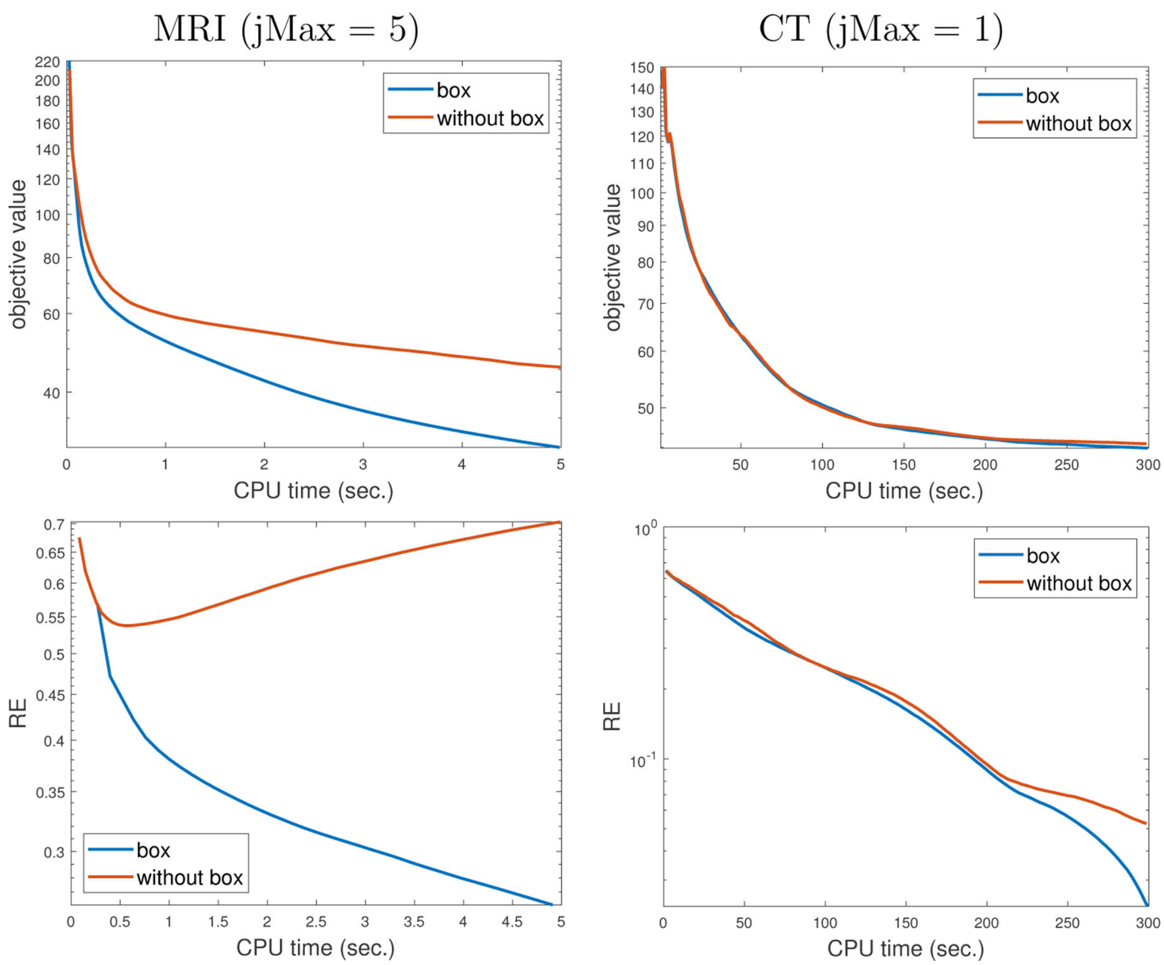

Figure 1.

The effects of box constraint on objective values (top) and relative errors (bottom) for MRI (left) and CT (right) reconstruction problems.

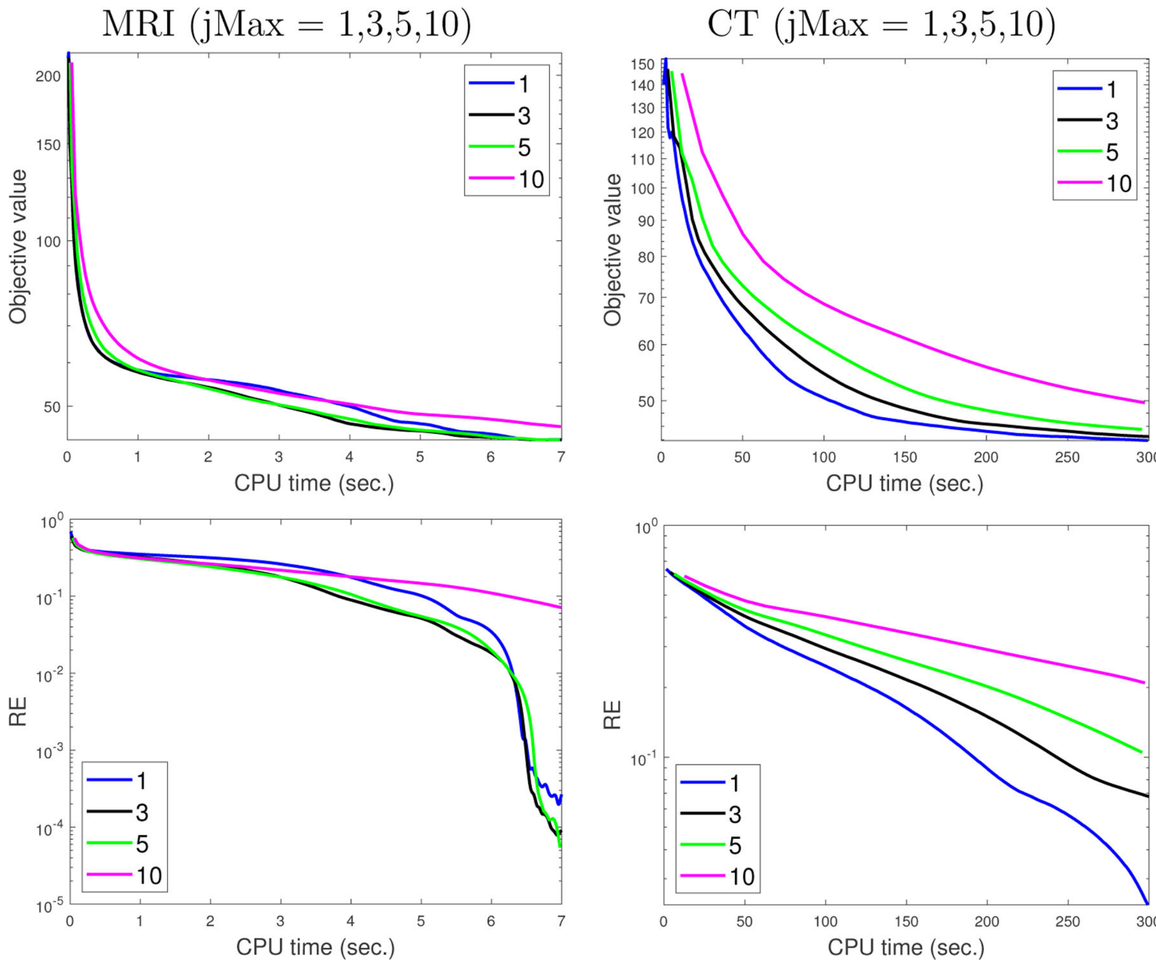

Figure 2.

The effects of the maximum number in the inner loops (jMax) on objective values (top) and relative errors (bottom) for MRI (left) and CT (right) reconstruction problems.

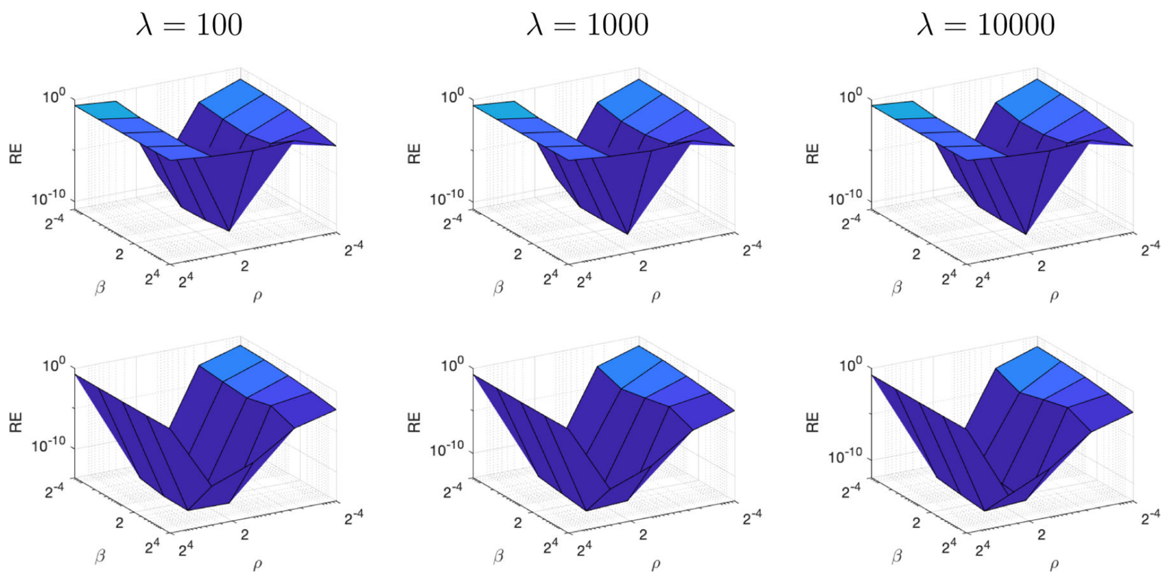

Figure 3.

The relative errors with respect to the parameters λ, ρ, β in Algorithm 1 for MRI reconstruction when kMax is 500 (top) or 1000 (bottom).

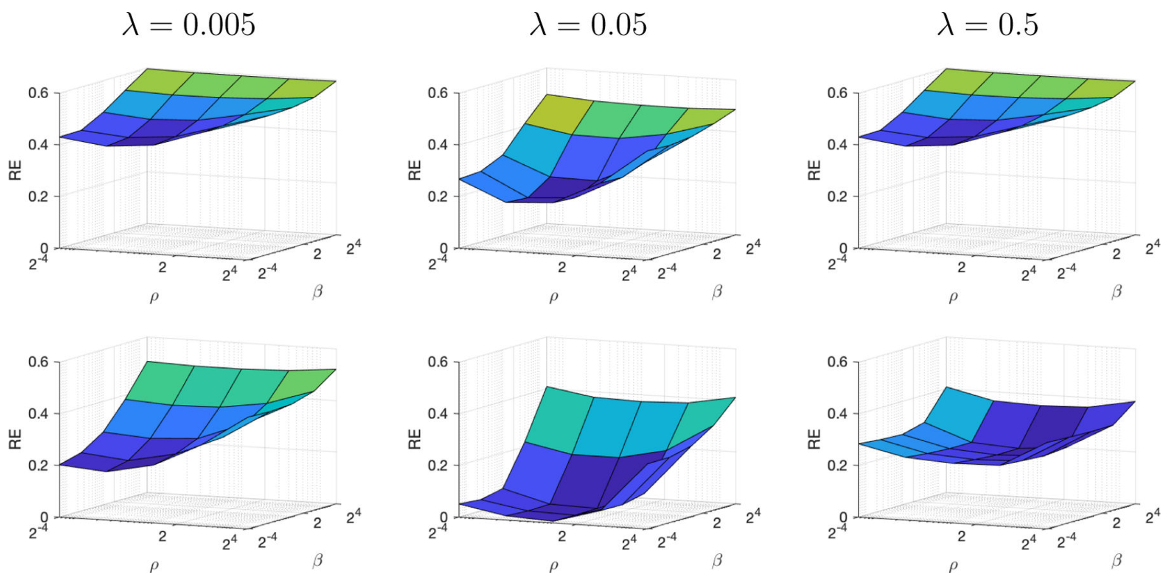

Figure 4.

The relative errors with respect to the parameters λ, ρ, β in Algorithm 1 for CT reconstruction when kMax is 100 (top) or 300 (bottom).

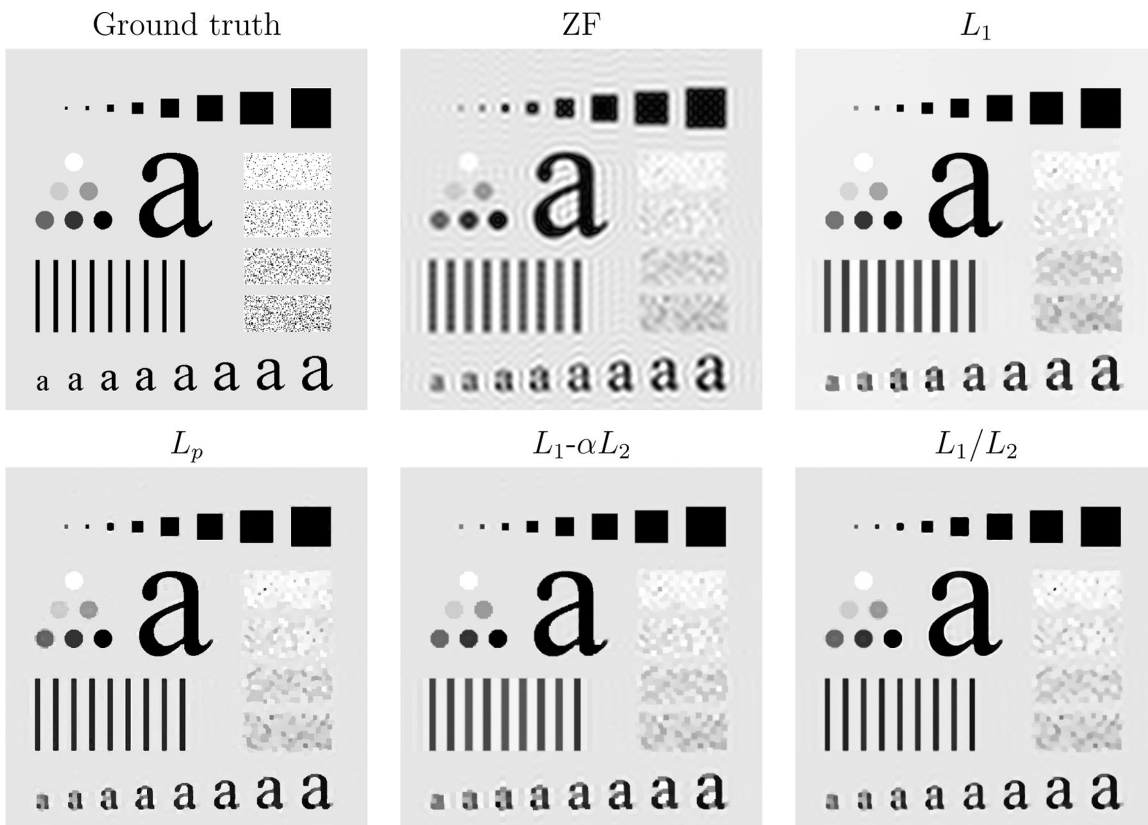

Figure 5.
Super-resolution from 1% low frequency data.

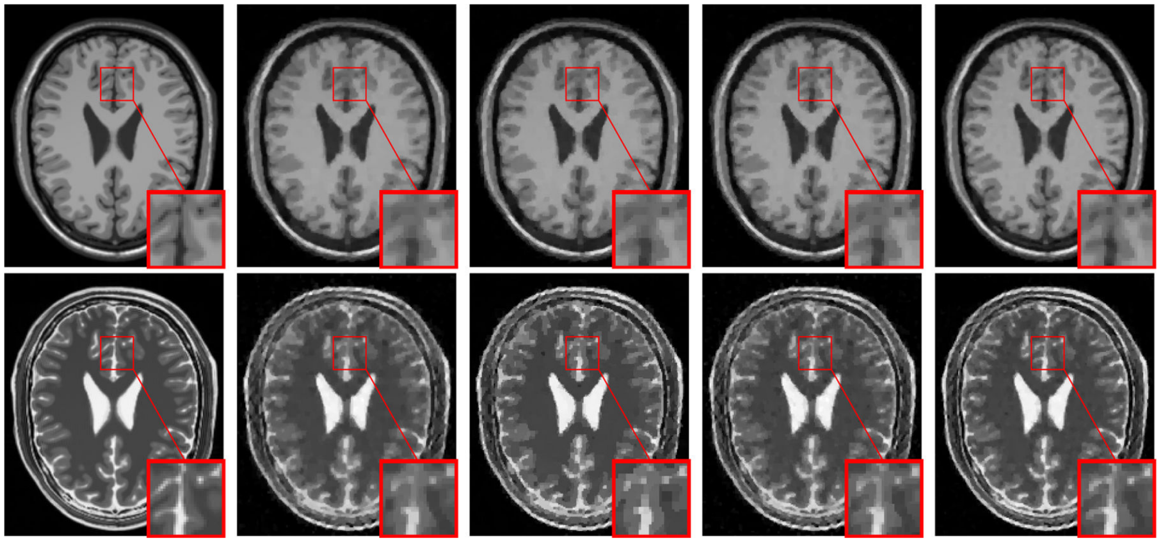

Figure 6.
MRI reconstruction from frequency measurements along 25 radial lines of T1 (top row) and T2 (bottom row). From left to right: ground truth, L_1, L_p, L_1-αL_2, and L_1/L_2.

Author Manuscript
Author Manuscript
Author Manuscript

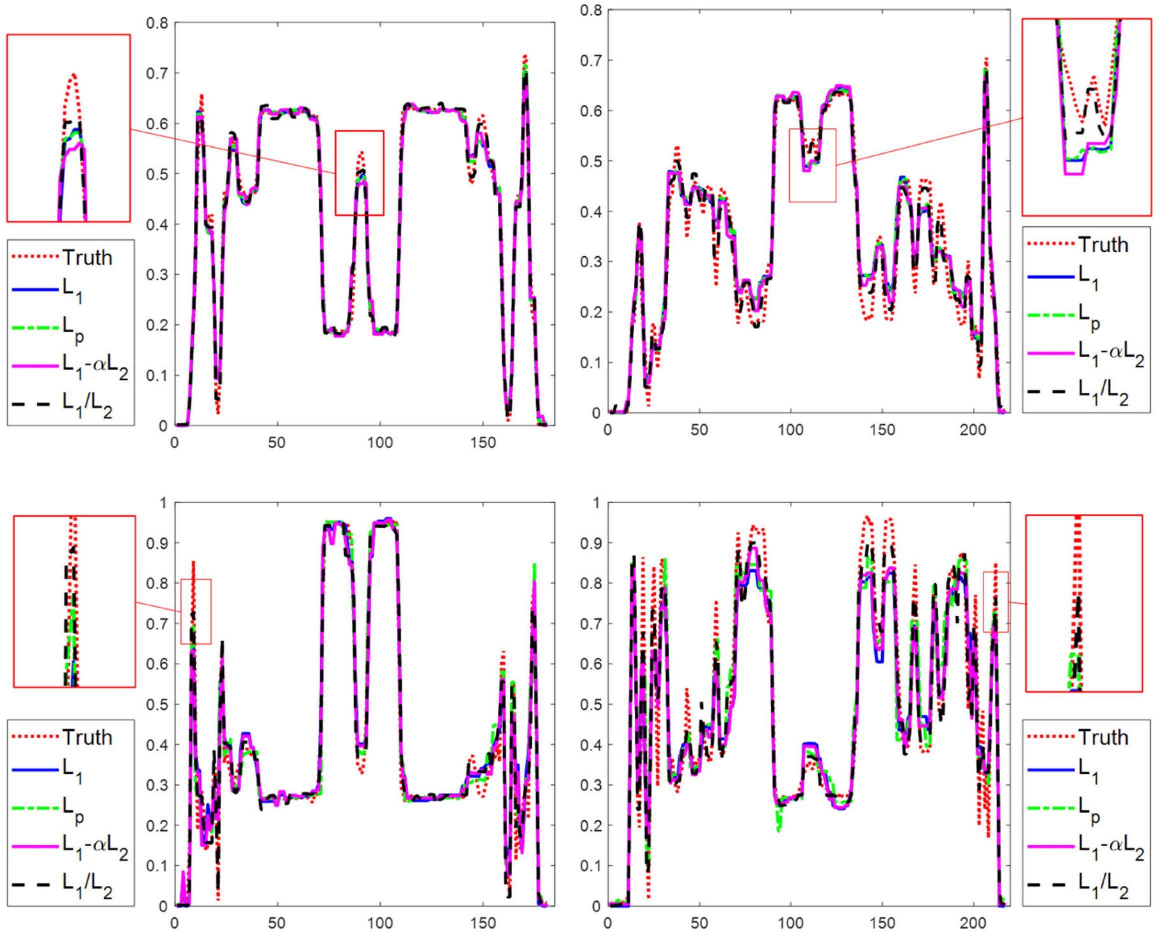

Figure 7.

Horizontal (left) and vertical (right) profiles of MRI reconstruction results from 25 radial lines for T1 (top) and T2 (bottom).

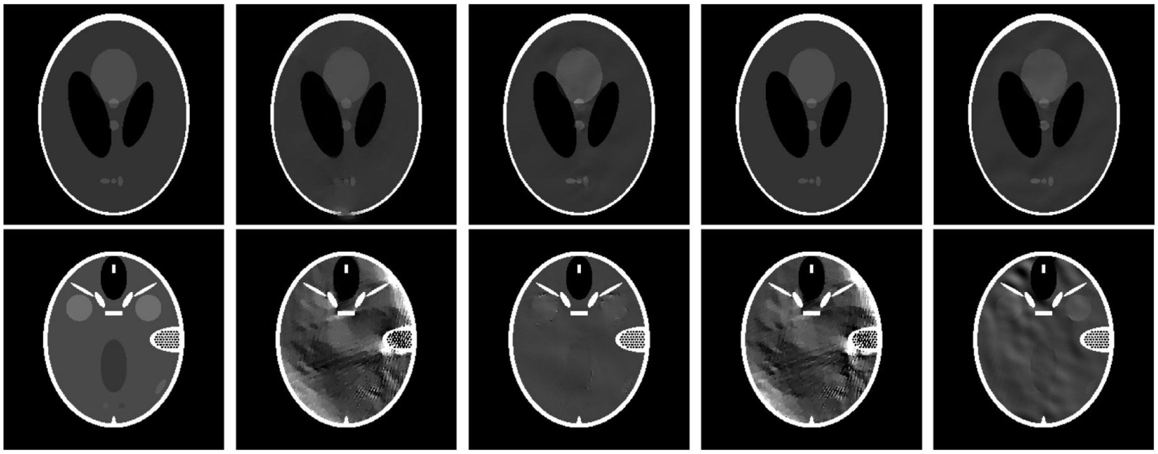

Figure 8.

CT reconstruction results of SL-45° (top) and FB-75° (bottom). From left to right: ground truth, L_1, L_p, L_1-αL_2, and L_1/L_2. The gray scale window is [0, 1] for SL and [1, 1.2] for FB.

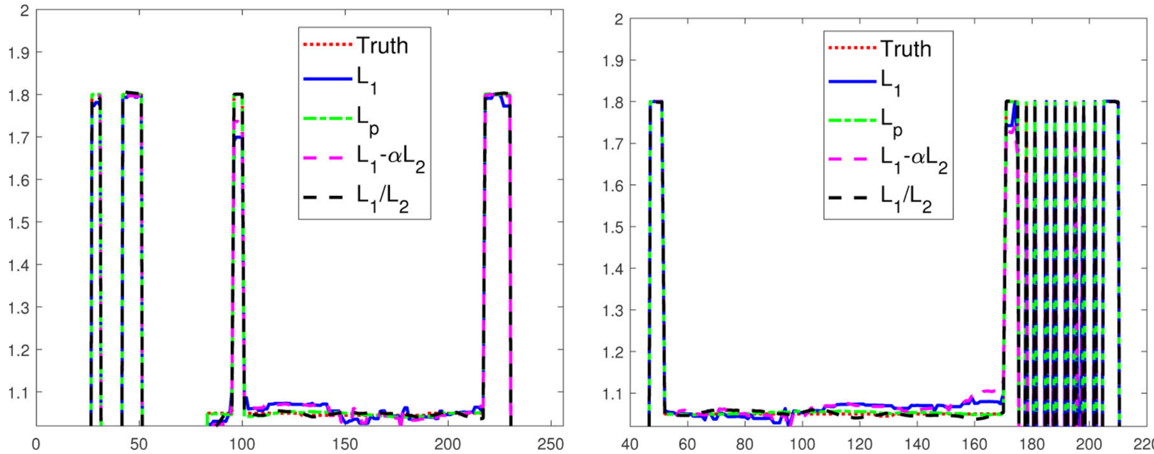

Figure 9.

Horizontal and vertical profiles of CT reconstruction results of FB-75°.

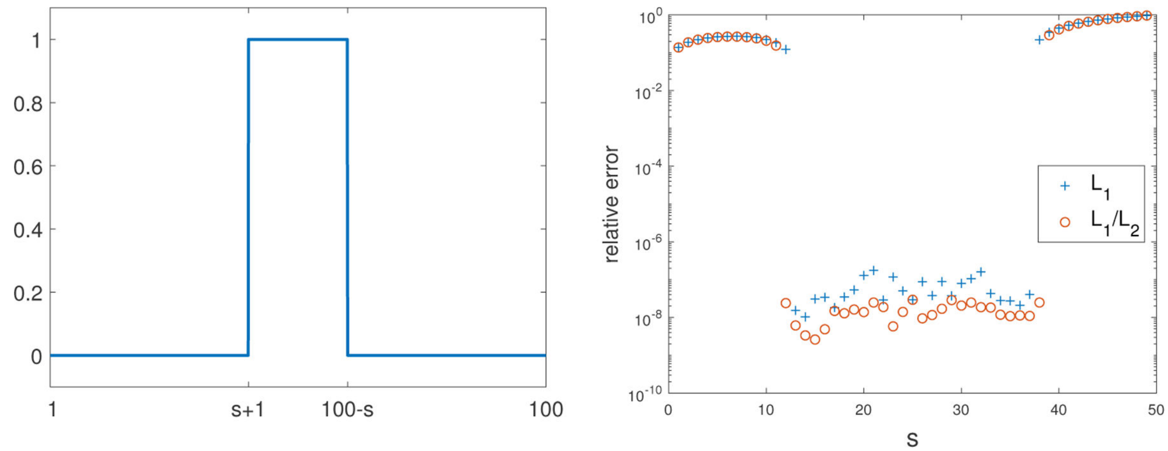

Figure 10.

A general setting of a one-bar step function (left) and reconstruction errors with respect to s (right) by minimizing L_1 or L_1/L_2 on the gradient. The exact recovery interval by L_1 is $s \in [13, 37]$, which is smaller than [12, 38] by L_1/L_2.

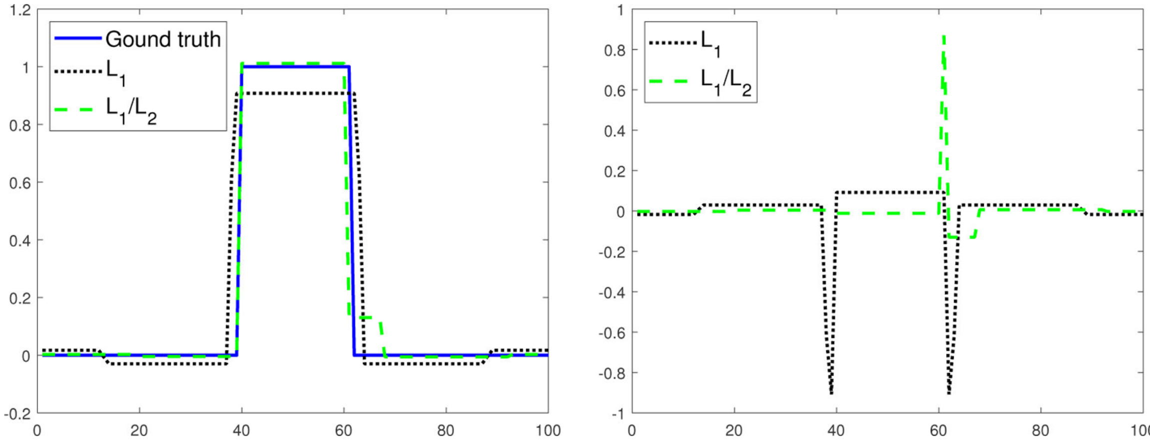

Figure 11.

A particular one-bar example (left) where both L_1 and L_1/L_2 models fail to find the solution. The different plot (right) highlights that L_1 results in larger oscillations compared to L_1/L_2.

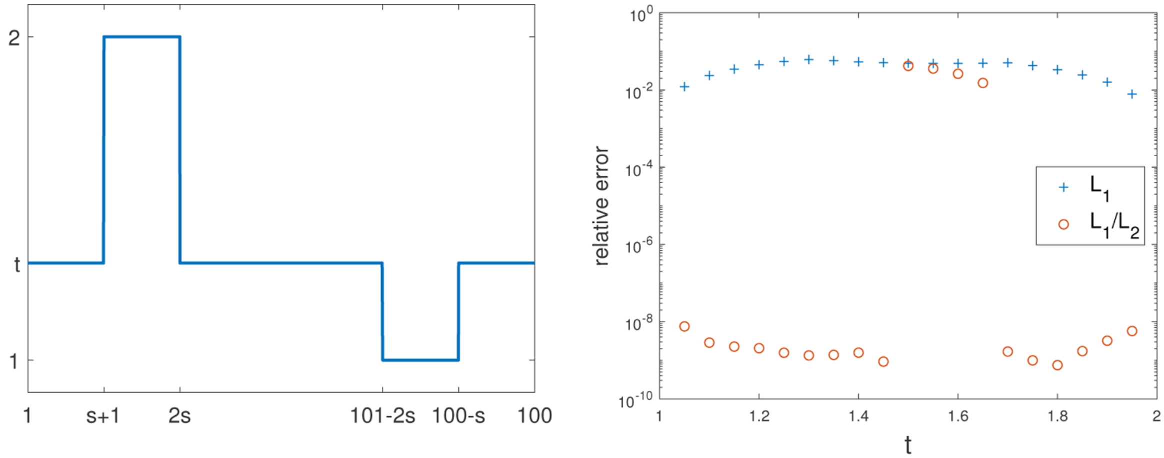

Figure 12.

A general setting of a two-bar step function (left) and reconstruction errors with respect to t (right) by minimizing L_1 or L_1/L_2 on the gradient, showing that L_1/L_2 is better at preserving image contrast than L_1 (controlled by t).

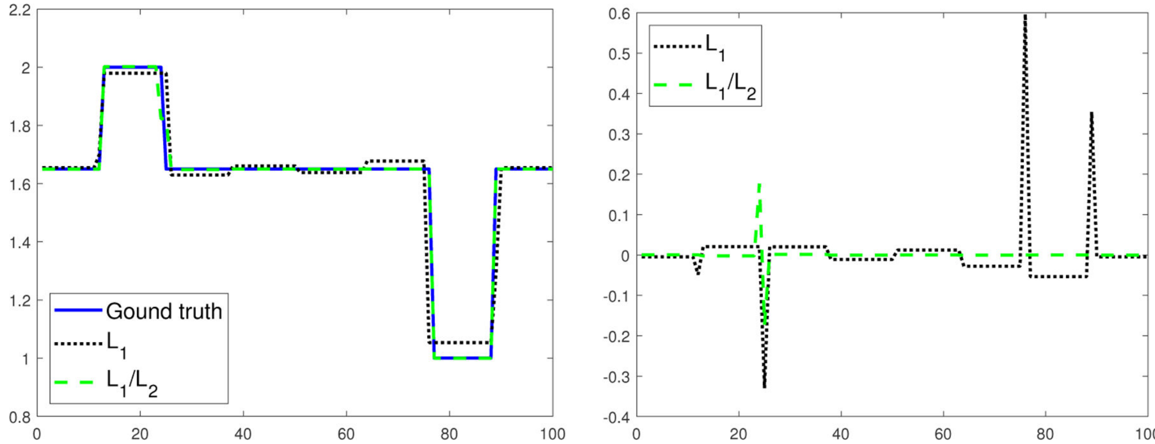

Figure 13.
A particular two-bar example where both L_1 and L_1/L_2 models fail to find the solution. The different plot is shown on the right.

Table 1.

MRI reconstruction from different numbers of radial lines.

Image	Line	ZF		L_1		L_p		L_1-αL_2		L_1/L_2	
		PSNR	RE	PSNR	RE	PSNR	RE	PSNR	RE	PSNR	RE
T1	20	21.26	22.13%	27.20	11.17%	27.24	11.11%	27.41	10.90%	29.94	8.15%
	25	23.42	17.26%	30.32	7.80%	30.06	8.04%	30.34	7.78%	33.21	5.59%
	30	24.07	16.02%	31.92	6.48%	31.63	6.70%	31.70	6.65%	34.84	4.63%
T2	20	17.89	33.91%	21.12	23.37%	21.13	23.34%	21.74	21.75%	23.50	17.76%
	25	18.83	30.44%	22.92	18.99%	23.23	18.33%	23.59	17.58%	25.80	13.63%
	30	19.42	28.43%	24.27	16.26%	24.76	15.36%	25.10	14.78%	27.60	11.09%

Author Manuscript

Author Manuscript

Author Manuscript

Table 2.

CT reconstruction with difference ranges of scanning angles.

phantom	range	SART		L_1		L_p		L_1-αL_2		L_1/L_2	
		PSNR	RE	PSNR	RE	PSNR	RE	PSNR	RE	PSNR	RE
SL	30°	15.66	66.95%	28.32	15.57%	40.25	3.95%	38.15	5.02%	60.77	0.37%
	45°	16.08	63.78%	33.33	8.75%	44.06	2.54%	63.34	0.28%	70.42	0.12%
	60°	16.48	60.92%	43.37	2.75%	46.50	1.92%	80.19	0.04%	73.46	0.09%
FB	60°	15.61	40.16%	25.43	12.96%	58.01	0.30%	26.24	11.81%	46.97	1.09%
	75°	16.14	37.79%	28.84	8.76%	59.02	0.27%	29.49	8.13%	49.30	0.83%
	90°	16.64	35.68%	69.68	0.08%	62.05	0.19%	75.67	0.04%	70.57	0.07%